AGU PUBLICATIONS

JGR

Journal of Geophysical Research: Atmospheres

RESEARCH ARTICLE
10.1002/2015JD024456

Key Points:
- Information about nocturnal opaque ice cloud optical depth available in multispectral infrared data
- Neural network algorithm developed to retrieve ice cloud optical depth from nighttime imager data
- Total cloud optical depth can be estimated from neural net ice COD using a parameterization

Correspondence to:
P. Minnis,
p.minnis@nasa.gov

Citation:
Minnis, P., G. Hong, S. Sun-Mack, W. L. Smith Jr., Y. Chen, and S. D. Miller (2016), Estimating nocturnal opaque ice cloud optical depth from MODIS multispectral infrared radiances using a neural network method, *J. Geophys. Res. Atmos.*, *121*, 4907–4932, doi:10.1002/2015JD024456.

Received 4 NOV 2015
Accepted 22 APR 2016
Accepted article online 26 APR 2016
Published online 12 MAY 2016

Estimating nocturnal opaque ice cloud optical depth from MODIS multispectral infrared radiances using a neural network method

Patrick Minnis[1], Gang Hong[2], Szedung Sun-Mack[2], William L. Smith Jr.[1], Yan Chen[2], and Steven D. Miller[3]

[1]NASA Langley Research Center, Hampton, Virginia, USA, [2]Science Systems and Applications, Inc., Hampton, Virginia, USA, [3]Cooperative Institute for Research in the Atmosphere, Ft. Collins, Colorado, USA

Abstract Retrieval of ice cloud properties using IR measurements has a distinct advantage over the visible and near-IR techniques by providing consistent monitoring regardless of solar illumination conditions. Historically, the IR bands at 3.7, 6.7, 11.0, and 12.0 μm have been used to infer ice cloud parameters by various methods, but the reliable retrieval of ice cloud optical depth τ is limited to nonopaque cirrus with $\tau < 8$. The Ice Cloud Optical Depth from Infrared using a Neural network (ICODIN) method is developed in this paper by training Moderate Resolution Imaging Spectroradiometer (MODIS) radiances at 3.7, 6.7, 11.0, and 12.0 μm against CloudSat-estimated τ during the nighttime using 2 months of matched global data from 2007. An independent data set comprising observations from the same 2 months of 2008 was used to validate the ICODIN. One 4-channel and three 3-channel versions of the ICODIN were tested. The training and validation results show that IR channels can be used to estimate ice cloud τ up to 150 with correlations above 78% and 69% for all clouds and only opaque ice clouds, respectively. However, τ for the deepest clouds is still underestimated in many instances. The corresponding RMS differences relative to CloudSat are ~100 and ~72%. If the opaque clouds are properly identified with the IR methods, the RMS differences in the retrieved optical depths are ~62%. The 3.7 μm channel appears to be most sensitive to optical depth changes but is constrained by poor precision at low temperatures. A method for estimating total optical depth is explored for estimation of cloud water path in the future. Factors affecting the uncertainties and potential improvements are discussed. With improved techniques for discriminating between opaque and semitransparent ice clouds, the method can ultimately improve cloud property monitoring over the entire diurnal cycle.

1. Introduction

Clouds comprise a key component of weather and climate. They alter the flow of solar and infrared radiation through the atmosphere between the surface and space, they serve as the source of precipitation, and their disappearance or formation affects the local sensible and latent heat balance. Because cloud processes occur throughout the diurnal cycle, it is critical for weather and climate models to accurately account for clouds both day and night. Numerical models require observations to develop parameterizations based on understanding of the processes and to validate the results [e.g., *Fridlind et al*., 2012]. Additionally, direct assimilation of cloud properties, such as cloud optical depth or water path [*Jones et al*., 2013, 2015; *Chen et al*., 2015], in weather models can demonstrably improve forecasts of critical parameters. The optimal source of cloud parameters for these weather and climate applications is satellite imager data, which provide contiguous spatial coverage and in the case of geostationary satellites, relatively continuous temporal coverage. Remote sensing of cloud properties from imager data has developed dramatically since the beginning of the satellite era and today provides a wealth of information about clouds in near-real time from a variety of satellites [e.g., *Minnis et al*., 2008a]. Yet there remain significant limitations on what can be retrieved using current algorithms, thus restricting the utility of the satellite data for providing critical cloud property information for weather and climate applications.

A full suite of cloud parameters can be determined from a combination of solar and infrared channels on modern research and operational satellite imagers [e.g., *King et al*., 2003; *Heidinger*, 2003; *Minnis et al*., 2011b]. These include cloud fraction, top height and temperature, visible (~0.65 μm) optical depth τ, and effective particle radius r_e, among other variables. The cloud water path (CWP) can be derived, with certain assumptions, from the product of τ and r_e. At night, using only a limited number of infrared channels, it is

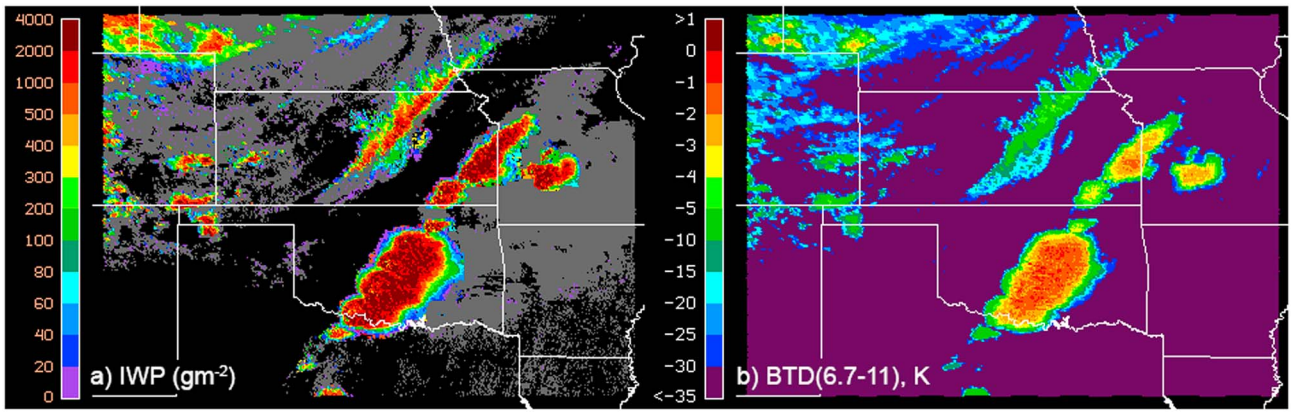

Figure 1. Parameters derived from GOES 13 over Southern Great Plains, 2015 UTC, 20 May 2013. (a) Ice water path and (b) brightness temperature difference between 6.7 and 11 μm channels.

possible to retrieve the same suite of variables, except that values of τ or r_e cannot be directly determined unless $\tau < 5$ or so [*Szejwach*, 1982; *Inoue*, 1985; *Liou et al*., 1990; *Lin and Coakley*, 1993; *Ou et al*., 1993; *Huang et al*., 2004; *Yue and Liou*, 2009; *Minnis et al*., 2011b]. Without the solar reflectance channels, the retrievals are limited to semitransparent clouds only. Nominally, the retrieval algorithms can decide if a cloud is opaque at infrared wavelengths [e.g., *Hong et al*., 2010a], but they cannot determine whether the cloud optical depth is 8 or 100, for example, due to a lack of definitive information within the infrared channel data. Thus, the use of those cloud properties and CWP for weather and climate applications has been confined to the daytime, a restriction that compromises the utility of the data. For example, a short-term forecast of convective storms based on assimilated satellite-retrieved values of CWP could be significantly degraded at night if the estimate of CWP is an assigned default value in the locations of important convective clouds and the near-storm environment [e.g., *Jones et al*., 2016].

The launch of the Suomi National Polar-orbiting Operational Environmental Satellite System (NPOESS) Preparatory Platform (SNPP) satellite with the Visible Infrared Imaging Radiometer Suite (VIIRS) has made it possible to retrieve opaque cloud optical depth using a day/night band (DNB) that measures reflected moonlight [*Walther et al*., 2013]. This exciting advance in cloud remote sensing is tempered by the complex nature of the sources contributing to the light received by the sensor, which include auroras, city lights, and fires [*Hillger et al*., 2013]—making the approach most useful over the global oceans at low to middle latitudes. Additionally, the intensity of the moonlight, though predictable [*Miller and Turner*, 2009], is highly variable and is near zero for roughly half of the lunar cycle as viewed from the SNPP orbit. Thus, despite its great potential, the DNB channel cannot be used to continuously monitor the optical properties of optically thick clouds at night. A different approach is needed to provide a more comprehensive solution.

Minnis et al. [2012] demonstrated that brightness temperatures (BT) and brightness temperature differences (BTD) at certain infrared wavelengths are sensitive to variations in τ and r_e for values of τ up to 20 and possibly even to higher values of ~100. These wavelengths, 3.7, 6.7, 8.5, 10.8, and 12.0 μm, are similar to those among the channels on board most current satellite imagers such as the Moderate Resolution Imaging Spectroradiometer (MODIS). A hint of the sensitivity and correlation of the data is evident in Figure 1, which shows the ice water path (IWP) and BTD between the 6.7 and 11 μm channels determined from the eastern Geostationary Operational Environmental Satellite (GOES) imager data over the Southern Great Plains during a daytime hour. The IWP was retrieved with the method of *Minnis et al*. [2011b]. There is clearly some relationship between the two parameters, but it does not appear to be a singular function. *Minnis et al*. [2012] found dependencies of BTD(6.7–11) on τ for a deep convective cloud case, but because the radiance sensitivities to τ are quite small, especially for $\tau > 20$, the relationship can easily be lost in the measurement noise and model uncertainties. Furthermore, BT and BTD values are not always sensitive to optical depth for opaque clouds. Thus, a direct approach based on modeling the radiance fields is impractical for retrieving nocturnal opaque ice cloud properties.

One method that skirts the need for a physical retrieval is the neural network. *Kox et al*. [2014] developed a neural network method to determine τ and cloud top height Z_t for nonopaque ice clouds using seven

infrared channels as input and τ from the Cloud-Aerosol Lidar with Orthogonal Polarization (CALIOP) on the Cloud-Aerosol Lidar and Infrared Pathfinder Satellite Observation (CALIPSO) [see *Winker et al*., 2007] satellite as output. That algorithm, applicable only to ice clouds having $\tau < 2.5$, proved quite successful at reproducing the CALIOP-based retrievals of τ and Z_t from passive infrared data. In earlier preliminary studies using MODIS data for input and retrievals based on CALIOP and CloudSat [*Stephens et al*., 2002] Cloud Profiling Radar (CPR) [*Im et al*., 2005] data for output, *Hong et al*. [2010b, 2012] found that a neural network approach might provide a reasonable estimate of τ for opaque ice clouds because it can simultaneously utilize the small amount of information available from each channel. This method, however, has not yet been fully documented and analyzed in detail. Nevertheless, it is clear that the neural network technique could prove valuable in overcoming, to some extent, the apparently inherent limitations of using only infrared data for cloud retrievals.

To address the need for obtaining reliable cloud optical depth information at night, this paper expands on the initial work of *Hong et al*. [2010b, 2012] and *Minnis et al*. [2010a, 2011a] to document and further develop this prototype method for using a neural network to estimate τ for opaque ice clouds from multispectral infrared brightness temperatures and their differences. Here the target output values consist of ice cloud optical depths from CPR data, because they are available both day and night and the CPR retrievals serve as optimal reference sets for training the neural network. Multispectral infrared data from MODIS are used as input to train the neural network to estimate τ. Because the channel complement differs from imager to imager, the technique, referred to as the Ice Cloud Optical Depth from Infrared using a Neural network (ICODIN), is tested using different combinations of channels centered near 3.7, 6.7, 10.8, and 12.0 μm. The method is assessed using independent CPR data as well as daytime retrievals using the MODIS visible channel and nighttime retrievals using the DNB from VIIRS. The potential uses and pitfalls of the ICODIN are then discussed.

2. Data

The ICODIN is developed to complement nocturnal retrievals that retrieve cloud properties for nonopaque clouds. The input data consist of multispectral radiances from passive imaging radiometers that are assumed to be associated with optically thick, i.e., opaque, ice clouds. The output data are optical depths derived from the active sensor.

2.1. Passive Satellite Data

Nocturnal brightness temperatures from 1 km Aqua MODIS channels 20 (3.7 μm), 27 (6.7 μm), 31 (11.0 μm), and 32 (12.0 μm) from March and October of 2007 and 2008 are used as the input for the ICODIN. The brightness temperatures of those channels and the 8.5 μm channel are included among the results of an intermediate step in the processing of the A-Train CALIPSO, CloudSat, Clouds and the Earth's Radiant Energy System (CERES), and MODIS merged product (C3M) [see *Kato et al*., 2010, 2011]. CERES is the Clouds and Earth's Radiant Energy System [*Wielicki et al*., 1998] project. The C3M processing matches up to three CALIPSO footprints with each MODIS pixel along its ground track. It then assigns the nearest CloudSat footprint to each of those MODIS pixels. The cloud properties from MODIS, retrieved using the algorithms of *Minnis et al*. [2011b], are included with the matched CALIPSO and CloudSat products along with radiances from 18 MODIS channels. Those matched data, constituting part of the C3M intermediate product, are used here. The CloudSat ground track is parallel to Aqua and is viewed by MODIS at viewing zenith angles (VZA) up to 18°. No corrections are made for parallax effects because of the small differences in VZA. Night is defined here as the solar elevation being at least 3° below the horizon, that is, at solar zenith angles exceeding 93°.

One Aqua MODIS image granule from July 2012 is used for comparison of ICODIN results with matched SNPP VIIRS DNB retrievals because VIIRS lacks the 6.7 μm channel. Another Aqua MODIS granule from 2007 is used for a daytime comparison with the ICODIN output.

2.2. Active Satellite Data

A large sample of data representative of the input and output parameters in the retrieval process is needed to train the neural network method. The primary output parameter here is ice cloud optical depth (ICOD). Neither CALIPSO nor CloudSat alone is sufficient for providing a complete picture of opaque cloud vertical structure. The CPR tends to miss thin clouds composed of small cloud particles (the minimum detection is −30 dBZ [*Stephens et al*., 2008]) particularly those at the tops of opaque ice clouds. The CALIOP signal detects

the ice crystals at cloud top missed by the CPR but is completely attenuated by optically thick clouds ($\tau > 3$) [*Kato et al*., 2010]. Therefore, the combination of CloudSat and CALIPSO data would provide the most complete cloud vertical profile. However, since the CALIOP typically measures an additional optical depth of only ~0.3 or less above the tops of opaque ice clouds determined from the CPR [e.g., *McGill et al*., 2004] and the minimum τ of 8 is the target here, then the exclusion of the extra τ from CALIOP adds a potential underestimate of the total ice τ value of 1–12% depending on the total depth of the cloud. However, much larger relative biases could occur for clouds with $\tau < 8$. In those instances, CloudSat could underestimate ICOD by 50% for $\tau = 2$. Nevertheless, given potential biases of up to 25% in the CloudSat retrievals [*Austin et al*., 2009], the absence of the CALIOP contribution to the total ICOD should have minimal impact on the estimates of truly opaque ice cloud τ values. Thus, the C3M CloudSat products are used alone to compute τ. The profiles of IWC and r_e in C3M are from the CloudSat L1B Release 4 2B-CWC-RO product [*Austin et al*., 2009], which includes three types of vertical profiles of ice water content (IWC) that make different assumptions about the temperature dependence of cloud particle phase. This study uses the profile type which assumes that all hydrometeors above the altitude corresponding to −20°C are ice phase and below the level corresponding to 0°C are liquid. Between the 0° and −20°C levels, the proportion of ice increases linearly from 0 to 100% with decreasing temperature.

To obtain the optical thickness of opaque ice clouds, the vertical profiles of IWC that are derived from CloudSat are used to estimate the total optical depth of ice clouds using

$$\tau_{\square\square} = \sum \frac{3}{4} \frac{\mathrm{IWC}}{r_e \rho} Q_e \Delta z, \tag{1}$$

where IWC and r_e are from CloudSat, ρ is ice particle density (0.917 g cm$_{)}^{-3}$ Δz is the vertical thickness of the ice cloud, and Q_e, the extinction coefficient for ice clouds, is given a value of 2 in this study.

The C3M global matched MODIS and CloudSat data from March and October 2007 are used as the training set. The March and October 2008 global matched data comprise the independent validation data set.

3. Methodology

To effect a retrieval using the neural network for opaque ice clouds, it is necessary to define what is opaque and determine which clouds meet that definition. Theoretically, the visible optical depth τ is approximately 2 times the infrared optical depth. Thus, the nadir view emissivity ε of a plane-parallel homogeneous cloud asymptotes to unity as τ increases from 4 ($\varepsilon = 0.865$) to 10 ($\varepsilon = 0.993$). Deciding at which emissivity the cloud is effectively opaque is somewhat arbitrary given that no cloud is truly plane parallel and homogeneous, and the inference of the emissivity is subject to considerable error. For this study, it is assumed that an opaque cloud has an emissivity equal to or greater than 0.982, which corresponds to $\tau = 8$ at nadir. However, the ICODIN must operate independently from the CPR data, and therefore, it is necessary to select data corresponding to $\tau_{CS} \geq 8$ using only the imager data. The available methods as well as the CPR retrieval are subject to significant uncertainties and therefore may not always select the same data. In recognition of those shortcomings, the training is performed using one passive method and an "ideal" method to select which pixels correspond to opaque clouds. The latter assumes that the pixels having $\tau_{CS} \geq 8$ can be selected without error, while the former selects pixels based entirely on what the passive technique indicates are opaque clouds. Additionally, a second passive method is used in the application of the ICODIN to evaluate the sensitivity of the results to the method employed for selecting opaque clouds. Nominally then, the ICODIN is applicable for ice cloud optical depths above 8. The maximum τ that can be retrieved is based on the selection criteria and the apparent limits of the information [*Minnis et al*., 2012]. As the results will show, the minimum can be quite different from the nominal value of 8 and the method can occasionally yield τ values as large as 150.

3.1. Opaque Ice Cloud Selection From Imager Data

The primary passive method used here for selecting opaque ice cloud pixels from MODIS data to develop the initial version of the ICODIN uses the 6.7, 8.5, 11, and 12 μm channels. The procedure combines the bispectral technique of *Baum et al*. [2000] and the trispectral technique of *Choi et al*. [2007] to identify ice clouds. The bispectral technique determines ice phase by satisfying either of the two tests: BT(8.5) ≤ 238 K or BTD(8.5–11) ≥ 0.5 K [*Baum et al*., 2000; *Menzel et al*., 2006], while the trispectral technique determines ice phase by satisfying one of the three tests: BT(11) ≤ 238 K, BTD(11–12) ≥ 4.5 K, or BT(6.7) ≤ 234 K.

Once classified as an ice cloud, the technique of *Hong et al*. [2010a] is used to classify the cloud as being opaque ($\tau \geq 8$) or semitransparent. These three approaches comprise the primary passive method used for training and are collectively denoted here as the Baum/Choi/Hong (BCH) technique. The ideal method requires that optical depths from BCH and from CloudSat are greater than or equal to 8 for both training and application.

The alternate approach for examining the sensitivity of the results to the passive method of opaque ice cloud selection is the standard CERES method for retrieving cloud properties at night, the Shortwave-infrared Infrared Split-window Technique (SIST) [*Minnis et al*., 2011b]. The SIST uses BT(3.7), BT(11), and BT(12) to retrieve phase, T_c, τ, and r_e, where T_c is the effective radiating temperature of the cloud, typically corresponding to an optical depth of ~1 below the geometric cloud top for optically thick clouds [*Minnis et al*., 2008b]. The SIST attempts retrievals up to $\tau = 16$, in some cases, but more often, it classifies the cloud as opaque and assigns default values of 8, 16, or 32 to clouds deemed as such. Here it is used only for independent evaluation of the CODIN and not for training.

Because the ICODIN must operate independently from CloudSat, it is important to understand the shortcomings of both the input and output data sets. Even though the BCH or the SIST determines a pixel's cloud as being opaque ice, CloudSat could have a different classification. In a comparison with the CALIOP phase classification for single-layered clouds, it was found that the SIST agreed with CALIPSO 94% of the time over snow and ice-free areas and 88% of the time over snow and ice-covered areas [*NASA*, 2015]. Compared with CloudSat and CALIPSO data, the BCH correctly identifies ~81% of the sampled upper tropospheric clouds as either opaque or semitransparent [*Hong et al*., 2010a]. While a portion of the misclassified pixels here is likely to be optically thin clouds, the phase of some opaque clouds will be misclassified in the supercooled temperature range. For those BCH pixels classified as opaque ice and are actually thin ice according to the CPR retrieval, the BCH-trained ICODIN will tend to force the revised retrieval to yield $\tau < 8$.

Phase selection in the supercooled range is difficult for both radar and infrared methods. Thus, the assumptions made about cloud particle phase in the CWC-RO product are entirely temperature based and can either underestimate or overestimate the actual ice CWC and affect τ_{CS} accordingly. Retrieval of cloud properties in the presence of precipitation is a difficult problem due to the sensitivity of the radar to precipitation-sized particles [*Austin*, 2007]. Because most of the precipitation is in the lower part of the clouds, the sensitivity should have smaller impact on the ice CWC. The CloudSat optical depth depends on the retrieved profiles of CWC and r_e. *Deng et al*. [2013] found that r_e values from the CWC-RVOD product are 30–50% larger than in situ measurements, while the CWC retrievals were relatively unbiased. Since the CWC-RO and CWC-RVOD products are statistically the same [*Protat et al*., 2010], it can be concluded that the CWC-RO r_e likely suffers from similar biases. Thus, τ_{CS} could represent a significant underestimate of the actual ICOD. On the other hand, from a different set of in situ measurements, *Austin et al*. [2009] found that IWC was generally overestimated with much scatter, so that it would compensate somewhat for any overestimate of r_e. Confident quantification of the errors in all of these methods is not complete owing to the paucity of definitive information. At this time, it is safe to conclude that uncertainties in both the input and output data could introduce significant scatter in the results.

In addition to the BCH, the SIST was also applied for comparison. For 2007, the SIST classified ~0.55 million pixels as opaque ice ($\tau \geq 8$) having BT(11) < 260 K or ~11% of all pixels containing ice in some layer according to CloudSat. BCH classified 1.61 million pixels or ~23% as opaque ice for the same period. Of the SIST opaque ice pixels, the SIST and BCH shared 59%, leaving 0.22 million pixels classified as opaque ice by SIST and not by BCH. Conversely, the BCH classified as opaque ice 1.28 million pixels that were not similarly identified by the SIST. These two methods are clearly different and should provide a measure of the ICODIN sensitivity to selected pixels.

3.2. Imager Retrievals for Comparisons

Cloud properties were derived from one 2007 daytime MODIS granule using the Visible Infrared Shortwave-infrared Split-window Technique (VISST) [see *Minnis et al*., 2011b]. The SIST was used for selected granules to evaluate the performance of the ICODIN at night.

A nighttime SNPP VIIRS image granule was also analyzed using the SIST and VISST, but with the DNB substituting for the visible (0.65 μm) channel for the VISST retrieval. It was assumed that the cloud reflectance at 0.65 μm is the same for the DNB bandwidth so that the daytime reflectance model used by

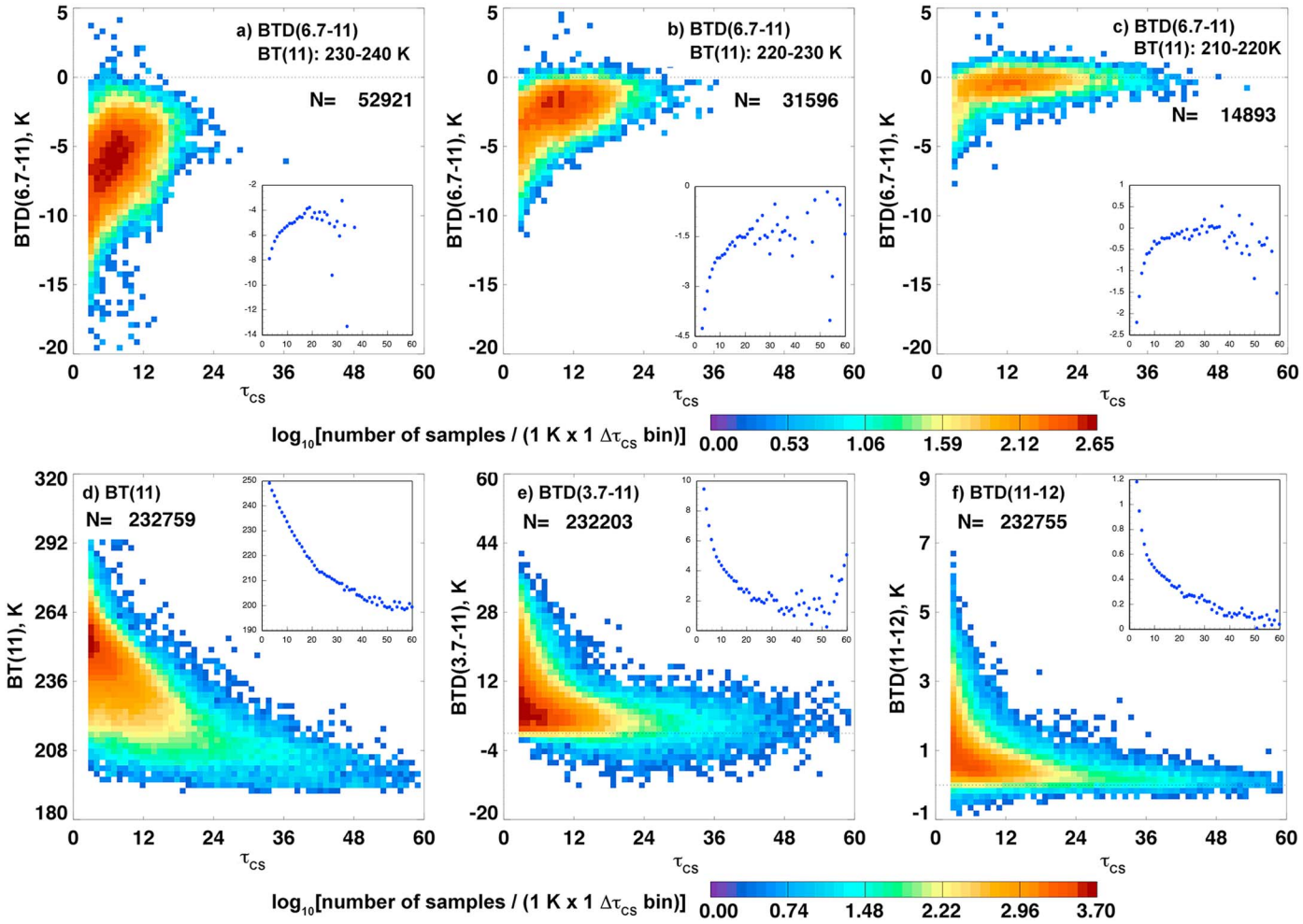

Figure 2. Frequency distributions of number of pixels having a particular pair of BT or BTD and τ_{CS} values for $\tau_{CS} > 2$ over nonpolar ocean, October 2010: (a–c) BTD (6.7–11) for different ranges of BT(11), (d) T11, (e) BTD(3.7–11), and (f) BTD(11–12). Insets show the mean thermal parameter as a function of τ_{CS}.

the VISST [*Yang et al.*, 2008] could be used at night. The DNB channel is much broader (0.5–0.9 μm) than the MODIS visible channel (0.615–0.678) so that some error will occur based on this assumption. The incoming moonlight intensity was computed using a revision of the model described by *Miller and Turner* [2009], which originally had an uncertainty of 7–11%. The uncertainty in the predicted lunar illumination from the revised model is between 5 and 10%.

3.3. Neural Network Retrievals

As noted in section 1, there are physical reasons why it might be possible to retrieve optical depths for opaque ice clouds using only a few infrared channels. To further illustrate the relationships between spectral infrared brightness temperatures and ICOD, Figure 2 plots the distribution of BT(11) and various BTDs as a function of τ_{CS} for all C3M data taken over water between 60°N and 60°S for the month of October 2010 using data having $\tau_{CS} > 2$. The insets in each panel show the mean values of the thermal parameter for each τ_{CS} bin. Figures 2a–2c show the dependence of BTD(6.7–11) for 3 BT(11) ranges. BTD(6.7–11) tends to increase with rising τ_{CS} for BT(11) between 230 and 240 K (Figure 2a) and starts to asymptote around $\tau_{CS} = 25$ for BT(11) between 220 and 230 K (Figure 2b) and for BT(11) between 210 and 220 K (Figure 2c) although the variation around zero tends to diminish as τ_{CS} rises further. For all of the data having $\tau_{CS} > 2$, the observed BT(11) decreases asymptotically as τ_{CS} approaches 60 (Figure 2d). The decreasing temperature implies a higher cloud top that, in turn, indicates the possibility for more cloud ice mass. While the scatterplots for BTD(3.7–11) in Figure 2e and for BTD(11–12) in Figure 2f do not seem to show decreasing values beyond $\tau_{CS} = 12$, the averages in the insets demonstrate that BTD(3.7–11) continues to decrease beyond $\tau_{CS} = 30$, with noisy results for

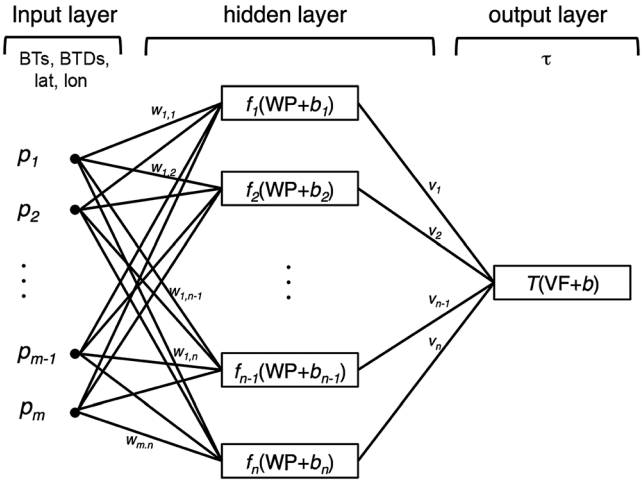

Figure 3. Schematic diagram of three-layer neural network used to determine opaque ice cloud visible optical depth τ.

$\tau_{CS} > 30$. The mean BTD(11–12) continues decreasing toward zero up to $\tau_{CS} = 60$. These plots are consistent, to some extent, with the theoretical calculations of *Minnis et al.* [2012], which reveal very small, monotonically diminishing differences in the BTD values of the three BTD combinations considered here. The computations of *Minnis et al.* [2012] show that BTD(3.7–11) is ~3 K for $\tau = 20$, decreases to ~1 K at $\tau = 60$, and approaches zero at $\tau = 150$. The mean in Figure 2e is very close to 3 K for $\tau_{CS} = 20$. The noise in BTD(3.7–11) for $\tau_{CS} > 30$ is due mostly to the drop in the 3.7 μm channel accuracy at low temperatures, as discussed in section 5, and likely masks the continuing decrease in BTD(3.7–11). From these results, it is clear that there is some small amount of information in each channel that appears to be lost in the noise but could possibly be exploited. By using information from all three BTDs and BT (11), it is hoped that ICOD can be estimated more accurately than possible with currently available methods (e.g., SIST).

Different from the direct retrieval of a parameter value using a representative physical model, neural network algorithms aim to identify the relationship between input and output variables by learning from a set of observed or simulated data [*Karayiannis and Venetsanopoulos*, 1993]. A neural network is a computer model composed of individual processing elements that are called neurons. The network can comprise multiple layers of neurons interconnected with other neurons in different layers that are referred to as the input, hidden, and output layers. The neurons are those neurons that receive signals from outside the neural network. Hidden neurons are between input and output neurons. They connect to both the input and output neurons. Output neurons combine the signals from the hidden layers and transmit signals to a receiver. The strength of the connection between two neurons is defined by a weight. The weights represent the memory of an artificial neural network and are used to determine the level of influence a given input has on the output layer. So the inputs are processed by a weighted summation function to produce a sum that is passed to a transfer function. The output of the transfer function is the output of the output neurons. A neural network constructs a nonlinear numerical model of a physical process in terms of network parameters that are trained with input and output parameters to determine the weights for any given connection.

Figure 3 shows the architectural graph of a three-layer perceptron with an input layer, a hidden layer, and an output layer. The neurons of the input layer are represented by vector $\boldsymbol{P}(p_1, p_2, \ldots, p_{m-1}, p_m)$, where m is the number of the input neurons or parameters. In the current study, $m = 10$ is used for the neural network training. The 10 neurons of $\boldsymbol{P}$ are BT(3.7), BT(6.7), BT(11), and BT(12), BTD(3.7–6.7), BTD(3.7–11), BTD(6.7–11), BTD (11–12), latitude, and longitude. The number of neurons in the hidden layer is determined during neural network architecture design and adjusted to produce best neural network performance. Here $n = 50$ neurons are used in the hidden layer for training. The number of neurons in the output layer is the number of output parameters in the retrieval. In this case, the opaque ice cloud optical depth τ, as indicated in Figure 3, is the lone output. The hidden layer weighting vector, $\boldsymbol{W}$, is given in the form of

$$\begin{pmatrix} w_{1,1} & w_{1,2} & \cdots & w_{1,n-1} & w_{1,n} \\ w_{2,1} & w_{2,2} & \cdots & w_{2,n-1} & w_{2,n} \\ \vdots & \vdots & \ddots & \vdots & \vdots \\ w_{m-1,1} & w_{m-1,2} & \cdots & w_{m-1,n-1} & w_{m-1,n} \\ w_{m,1} & w_{m,2} & \cdots & w_{m,n-1} & w_{m,n} \end{pmatrix},$$

where $w_{m,n}$ is the weight between input neuron, p_m, and hidden neuron, n. The output layer weighting vector, $\boldsymbol{V}(v_1, v_2, \ldots, v_{n-1}, v_n)$ comprises the weights between the hidden neurons and the output neuron. The vector, $\boldsymbol{B}(b_1, b_2, \ldots, b_{n-1}, b_n)$, is the bias in the hidden layer, and b is the bias in the output layer.

The network training function of Bayesian regulation backpropagation is used for the three-layer neural network. This training function updates the weight and bias values according to Levenberg-Marquardt optimization. It minimizes a combination of squared errors and weights and then determines the correct combination so as to produce a network that generalizes well. During the training, different transfer functions between the input and hidden layers and between the hidden and output layers were investigated. It was found through initial testing that using a log-sigmoid transfer function $s(x)$ to propagate to the hidden layer and a hyperbolic tangent sigmoid transfer function $t(x)$ to propagate to the output layer produces the optimal network performance. The log-sigmoid and the hyperbolic tangent sigmoid transfer functions, respectively, are

$$s(x) = \frac{1}{1 + \exp(-x)}, \tag{2}$$

and

$$t(x) = \frac{2}{1 + \exp(-2x)} - 1. \tag{3}$$

During initial trials using this approach, both r_e and τ were selected for output. However, no skill was found for estimating r_e, so as noted above, the analysis seeks only one output parameter, τ.

The training was performed for all MODIS pixels classified as opaque ice by the BCH method and having BT (11) $<$ 260 K, which is warmer than the center of the supercooled temperature range but substantially colder than the freezing level. Temperatures less than 260 K are often associated with thick ice clouds such as cirrus anvils or deep convective elements [e.g., *Tian et al*., 2004]. Additionally, the training was performed separately for pixels having BT(11) $<$ 250, 240, and 235 K, to determine if the skill could be improved by additional classification. This approach implicitly assumes that no optically thick ice clouds occur with top temperatures greater than 260 K.

The ICODIN was trained using four different combinations of channels: a four-channel method using BT(3.7), BT(6.7), BT(11), and BT(12) and relevant BTDs denoted as ICODIN4 and three 3-channel methods. The ICODIN3a, which uses BT(6.7), BT(11), BT(12), BTD(6.7–11), and BTD(11–12), is applicable day and night, while ICODIN3b, which uses BT(3.7), BT(11), BT(12), BTD(3.7–11), and BTD(11–12), can be used on sensors lacking a 6.7 μm channel. A third night-only version, ICODIN3c, uses BT(3.7), BT(6.7), BT(11), BTD(3.7–6.7), BTD(3.7–11), and BTD(6.7–11) and could be used for sensors lacking a 12 μm channel.

During the training, out of the total about 1.6 million collocated data for 2007 meeting the criteria listed earlier, one out of every three pixels was selected for the training process. Of those selected pixels, 60% were chosen randomly to comprise the training set, which was employed to compute the gradient and update the network weights and biases. Of the remainder, 20% were extracted for validation and 20% were used for testing. Computer memory limitations necessitated this downsizing of the data set. The independent 2008 data set included ~1.7 million pixels, which is roughly 34% of the total number of C3M pixels for the time period. After training, the ICODIN method was applied to all of the 2007 and 2008 data.

4. Results

Retrievals are presented for all versions of the ICODIN and for the SIST. Table 1 summarizes the six different methods compared here. Since the SIST is not a neural network algorithm, it requires no training.

4.1. Four-Channel Neural Network (ICODIN4) Training and Validation

To determine the optimal set of temperature thresholds for using ICODIN, histograms of τ from CloudSat and the four ICODIN4 training and validation runs were created and plotted as shown in Figure 4. CloudSat results are shown as black and red lines, while the various ICODIN4 results are shown as blue and green lines. Frequencies for $\tau < 50$ are shown in Figures 4a and 4b for BT(11) $<$ 260 and 235 K and for BT(11) $<$ 250 and 240 K, respectively. Similarly, Figures 4c and 4d show the corresponding results for optical depths between 30 and 150 on a different scale. The ICODIN and CloudSat distributions in Figure 4 are close, but not identical. The greatest divergences appear for $\tau < 10$ for BT(11) $<$ 260 and 250 K, for $\tau < 20$ for BT(11) $<$ 240 K, and between $\tau = 10$ and 20 for BT(11) $<$ 235 K. All of the curves drop off exponentially from $\tau < 2$. It is clear that many of "opaque" pixels as determined by the imager retrievals contain ice clouds having $\tau < 8$. Overall,

Table 1. Methods Tested for Estimating Opaque Ice Cloud Optical Depth[a]

Retrieval Method	Training Opaque Detection Method	Channels Used	Application Opaque Detection Methods
BCH ICODIN4	BCH	3.7, 6.7, 11, and 12 μm	BCH and SIST
ICODIN3a	BCH	6.7, 11, and 12 μm	BCH
ICODIN3b	BCH	3.7, 11, and 12 μm	BCH
ICODIN3c	BCH	3.7, 6.7, and 11 μm	BCH
SIST	NA	3.7, 11, and 12 μm	BCH and SIST
Ideal ICODIN4	BCH + $\tau_{CS} > 8$	3.7, 6.7, 11, and 12 μm	BCH + $\tau_{CS} > 8$

[a]NA: not available.

68% of the clouds identified as opaque ice by the BCH method were determined to be semitransparent ($\tau < 8$) by CloudSat. Similar results (48%) were found for the SIST method. This apparent misidentification by the BCH and SIST probably involves impacts of phase misclassification and optical depth errors in the imager retrievals, uncertainties in the CloudSat retrieval and assumed phase, and the occurrence of thin ice clouds over water clouds with only small or no vertical separation between the layers. That last condition would likely result in a false determination of opaque ice by one or both of the passive methods.

Here it is assumed that an optimal approach is that which would produce the same distributions of τ as observed by CloudSat. To determine the temperature threshold that yields the optimal statistical representation of the CloudSat ice cloud optical depths τ_{CS}, the ratio, $N(\tau_{CN4})/N(\tau_{CS})$, was plotted in Figure 5 for both the 2007 and 2008 results, where τ_{CN4} is the ICODIN4 optical depth and N is the number of samples in a given optical depth bin defined by either τ_{CN4} or τ_{CS}. The ratios for $\tau < 50$ and $\tau \geq 50$ for 2007 are plotted in Figures 5a and 5b, respectively. Their 2008 counterparts are shown in Figures 5c and 5d. For both 2007 and 2008, the ratio is closest to 1.0 for BT(11) < 260 K for τ between 8 and 50. For $\tau < 8$, all thresholds produce large errors, except for BT(11) < 235 K during 2007. For $\tau > 50$ (Figures 5b and 5d), the ratio drops almost linearly from near unity to near zero at $\tau = 150$, indicating much reduced skill for retrieving values of $\tau > 60$ using ICODIN4. The black curve is mostly on top for 2007 (Figure 5b), while the red curve appears to yield more for $\tau > 120$ or so for 2008 (Figure 5d). Considering the complexity in application and the evident uncertainties for each threshold, it was decided to use the training set for BT(11) < 260 K, except when the set for BT (11) < 235 K produces a value of $\tau > 110$. The latter set is used to maximize the retrieval of the larger optical depths. Although the ratios were near unity for BT(11) < 235 K and $\tau_{CS} < 8$, including those criteria in the method made no difference in the overall agreement with τ_{CS}. Thus, the combination of the two training sets noted above constitutes the method used hereafter for all forms of the ICODIN.

Figure 6 shows the relative importance of the different input parameters to ICODIN4 for the various temperature constraints as computed from the connection weights using the method of *Garson* [1991]. Latitude and longitude appear to be most important followed by BTD(11–12) and BTD(6.7–11). The other parameters mostly have relative weights of less than 10% with BT(11) and BTD(3.7–6.7) having the smallest values. This is surprising given the results in Figure 2. The weights change with temperature threshold by 20% or more.

The final training results using the four channels are shown as density scatterplots in Figure 7, where the bin size is one optical depth unit. For clarity, the results are plotted separately for $\tau_{CS} < 15$ (Figure 6a) and $\tau_{CS} \geq 15$ (Figure 6b). Note the different color bars used for the two plots. The goal of this study is to estimate τ for opaque ice clouds. Figure 6a reveals that semitransparent—as determined from CWC-RO—clouds are more common in this data set despite the best efforts of the BCH to identify opaque clouds. Nevertheless, ICODIN4 tends to assign more appropriate optical depth values to those "thin" opaque clouds. The data remain correlated for $\tau_{CS} \geq 15$ but are skewed. The results are very similar for the 2008 validation data set (not shown). For both 2007 training and independent 2008 results the correlation coefficients, R, between the τ_{CN4} and τ_{CS} values are 0.80 and 0.78, respectively. The bias for the training results is only −0.07 (−0.8%), while the 2008 bias is −0.10 (−1.2%). The corresponding standard deviations of the differences (SDD) are 99 and 105%. The accuracy of the ICODIN4 applied to the independent data set is only slightly degraded and, therefore, should be generally applicable to all MODIS data, at least, for those observations near nadir.

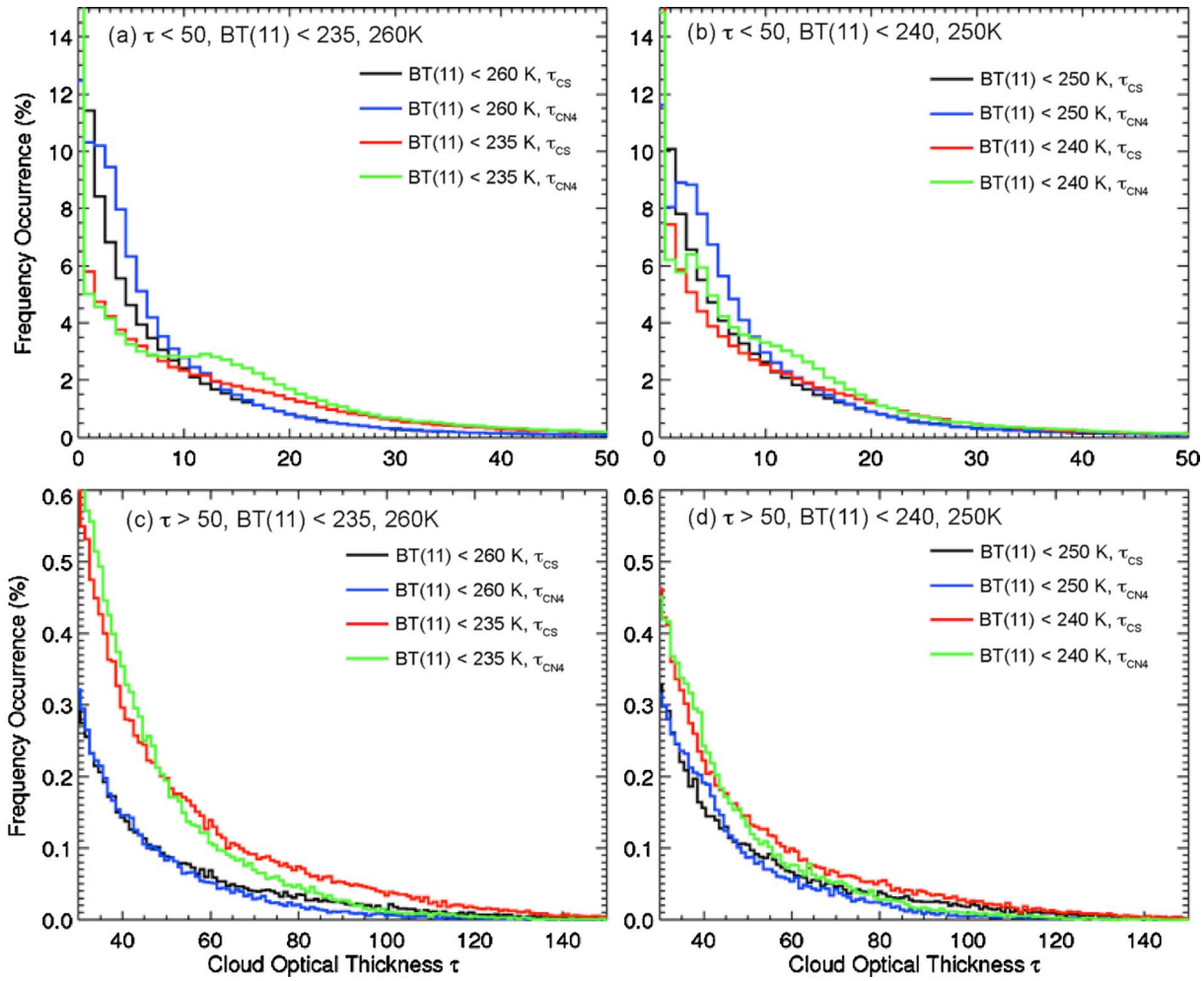

Figure 4. Probability distributions of 2007 global τ values retrieved from CloudSat data and from Aqua MODIS using ICODIN4 with four observed 11 μm brightness temperature thresholds. (bin size = 1). (a and b) For $\tau \leq 50$. (c and d) For $\tau > 30$.

The scatterplots for the ideal case (not shown) are similar in appearance except that they lack any pixels having $\tau < 8$. For the ideal cases, R is diminished to 0.73 and 0.71 for 2007 and 2008, respectively. The corresponding biases are −0.07 (0.3%) and −0.33 (1.5%). Substantial improvement was gained in the SDD values, which are 61% and 63% for 2007 and 2008, respectively. Given those statistics for the ideal cases, confining the true optical depth domain to $\tau > 8$ is preferable and, in application, will require better methods than are currently available for determining opaque clouds from the passive imagery.

The sample densities of scatterplots in Figure 7 do not coincide with the line of agreement. As expected from the results in Figure 5, the ICODIN4 results at the low end ($\tau < 15$) are mostly greater than the CPR values, while the opposite occurs at the high end. There, relatively few ICODIN4 values exceed 70; however, there are τ_{CN4} values as large as 100, but fewer than 5 (not shown) in a given optical depth pair. Thus, ICODIN4 tends to dampen the range but still yields a relatively high correlation. To determine if the results are imbalanced, the mean values of τ_{CN4} and τ_{CS} were computed for every 2.5 ICODIN4 optical depth intervals between 0 and 50 and for every five optical depth intervals for $\tau_{CN4} > 50$. Figure 8 shows the binned averages connected by a line. The means tend to follow the line of agreement up to $\tau_{CN4} \sim 70$ and then diverge with the 2007 and 2008 data going above and below the line, respectively. The divergence suggests that either the sample set is too small for the larger optical depths or the information content is diminished, or both. Given the trends in Figures 5b and 5d, it is likely that the information content is greatly diminished as τ increases beyond 50. However, these results show that on average, for any given value of $\tau_{CS} < 70$, τ_{CN4} is unbiased relative to τ_{CS}.

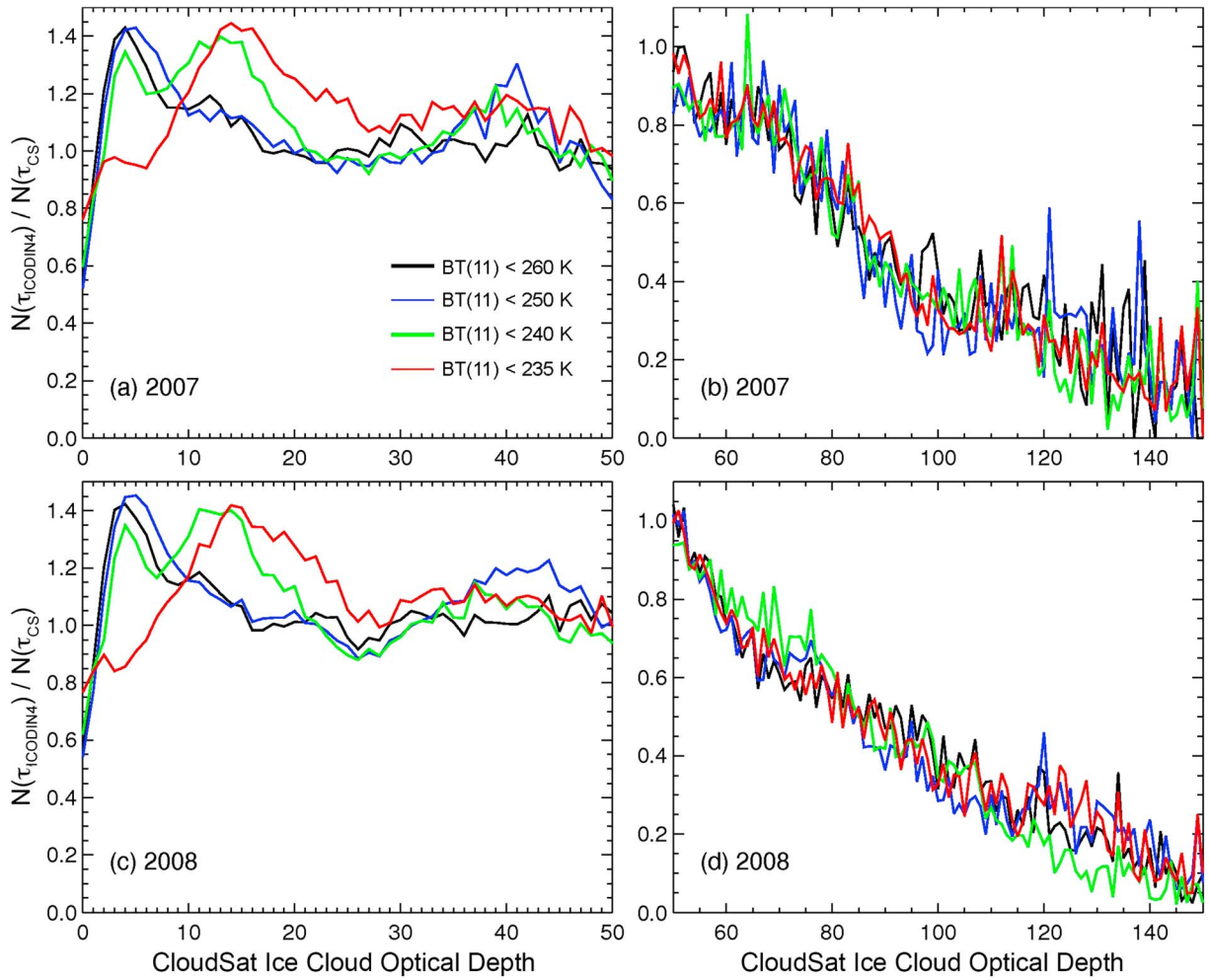

Figure 5. Ratio of occurrence frequencies of ICODIN4 optical depth to those of CloudSat optical depth for a given CloudSat ice cloud optical depth. Note the scale difference between left and right panels. (a and c) For $\tau \leq 50$. (b and d) For $\tau > 50$.

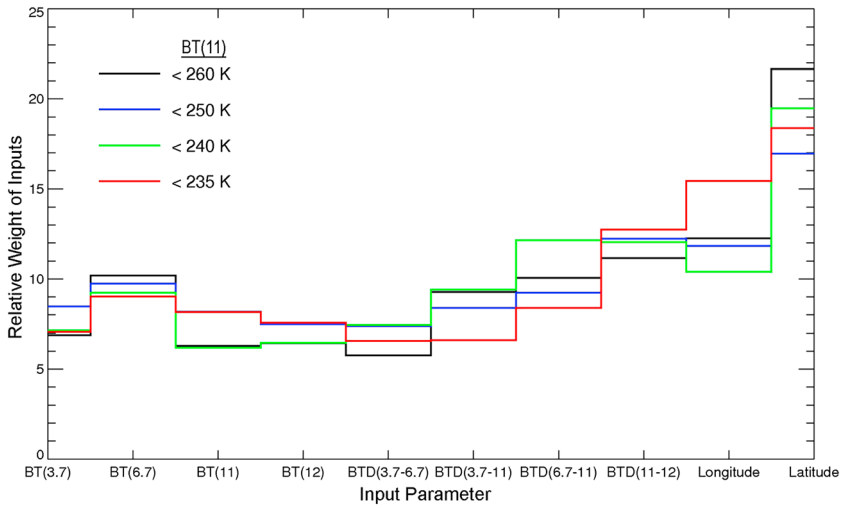

Figure 6. Relative weights of the input parameters for ICODIN4.

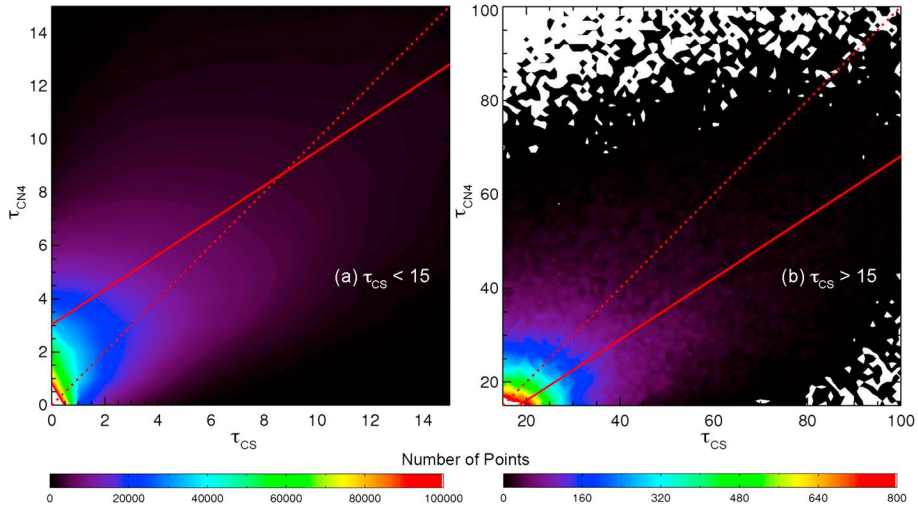

Figure 7. Density scatterplots of nocturnal opaque ice cloud optical depths retrieved from CloudSat and Aqua MODIS data using ICODIN4 from the 2007 training period for (a) $\tau_{CS} < 15$ and (b) $\tau_{CS} > 15$. BCH was used to determine opaque clouds. Solid line indicates linear regression fit. Dashed line is the line of agreement.

The damping effect of the neural network on the extreme values, suggested by Figure 5, can also be seen in regional averages. Figure 9 plots the average nighttime opaque ICOD for 2° latitude by 2° longitude regions from the CPR and from MODIS using ICODIN4. While the patterns are very similar, the CloudSat retrievals have more dark blue ($\tau < 3$) areas, especially in higher latitudes and more red ($\tau > 50$) regions, particularly in the tropics. The ICODIN4 means tend to be smoother than their CPR counterparts. Those same 2° × 2° regional averages are compared in a scatterplot (Figure 10), which shows that overall, the averages are unbiased and the mean regional difference could be as large as 65% at the one standard deviation level. It is clear from the plot that for many regions, the ICODIN4 overestimates the mean τ by 1−2 for $\tau < 3$ and underestimates the mean for $\tau > 15$.

Figure 11 shows an example of the ICODIN4 applied to MODIS data along the CloudSat ground track for a MODIS granule taken over the tropical eastern Pacific at 0830 UTC 25 July 2008. The track, shown as a line over the multispectral (Figure 11a) and BT(11) (Figure 11b) images, passes through areas of deep convection separated by low clouds. The line is black except over opaque ice clouds where it is red. The CPR reflectivity image for the ground track segment between 8°N and 14°N (Figure 11c) shows cloud tops reaching 15 km and a melting layer near 5 km with two deep cells around 10°N. The corresponding optical depths retrieved from the CPR and MODIS (ICODIN4) are plotted as blue and red points, respectively, in Figure 11d. Estimates of ICOD by the SIST alone, τ_{SIST}, are also shown as green points. Values of τ_{CN4} and τ_{CS} track well for much of the segment, but τ_{CN4} underestimates τ_{CS} for values exceeding 50. Those values are mostly greater than τ_{SIST}, which defaults to either 16 or 32 for many of pixels. Figure 11e compares τ_{CS} and τ_{CN4} for the ideal case. In this instance, the ICODIN4 follows CloudSat more closely and yields values of τ_{CN4} up to 105. ICODIN4 overestimates τ_{CS}

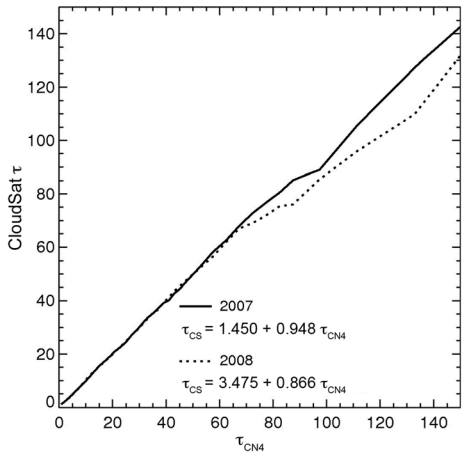

Figure 8. Mean bin opaque ice cloud optical depth from CPR retrieval as a function of ICODIN4 optical depth from 2007 training (solid) and 2008 validation results (dashed). Each bin corresponds to 2.5 ($\tau_{CN4} < 50$) and 5 ($\tau_{CN4} \geq 50$) ICODIN4 optical depth units.

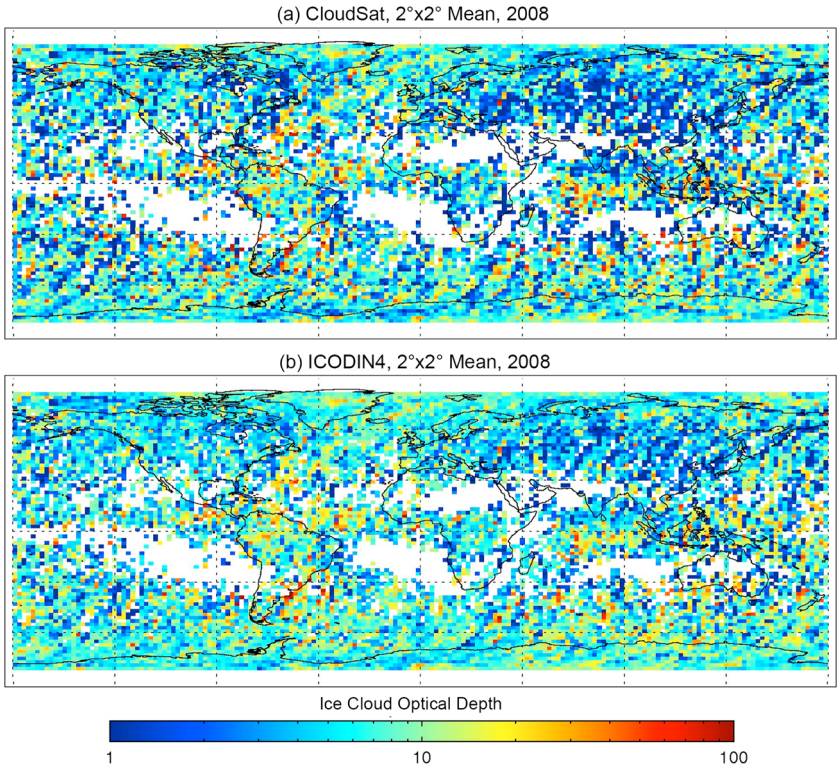

Figure 9. Geographical distribution of 2° × 2° regional mean opaque ice cloud optical thickness during nighttime in 2008 from (a) CloudSat CPR retrievals and (b) Aqua MODIS ICODIN4 retrievals.

on the edges of the convective clouds, where the clouds remain thick but likely have less ice. While the ideal case provides a more accurate ICOD for most of the opaque clouds, both results provide improved information about opaque ice clouds than any default values.

This can be seen clearly in Figure 12, which compares the results of the ICODIN4 and the SIST applied to the entire MODIS granule in Figure 11. Despite the lack of training at off-nadir VZAs, the ICODIN4 (Figure 11a) produces a very reasonable distribution of τ values compared to the images in Figures 11a and 11b. Few, if any pixels in the northwestern sector, have $\tau_{CN4} > 100$, while a large area of $\tau_{CN4} > 100$ is evident for the massive convective system near 6°N, 87°W, which is dominated by pixels having BT(11) < 200 K. It is not clear if these larger values are the result of VZA effects. Many of the pixels selected as opaque by the BCH yield $\tau_{CN4} < 8$ (black pixels). These distributions can be contrasted with the almost featureless SIST retrievals (Figure 12c) from the CERES Edition 4 analyses [*Minnis et al.*, 2010b] that have values of 32 for most of the colder clouds. If the SIST is used to select the opaque clouds for applying ICODIN4 (Figure 12b), fewer areas are selected as opaque clouds but some different areas (e.g., near 4°N, 92°W) are classified as opaque by the SIST. Most of the clouds that appear to be optically thick visually are selected by both methods.

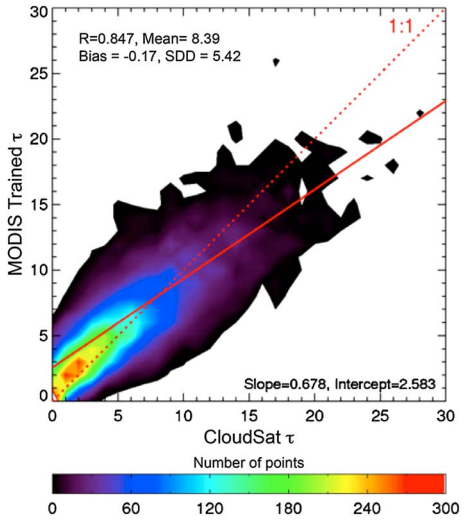

Figure 10. Density plots of the correlation between 2008 2° × 2° regional mean τ estimated from data in Figure 5 (bin size = 1).

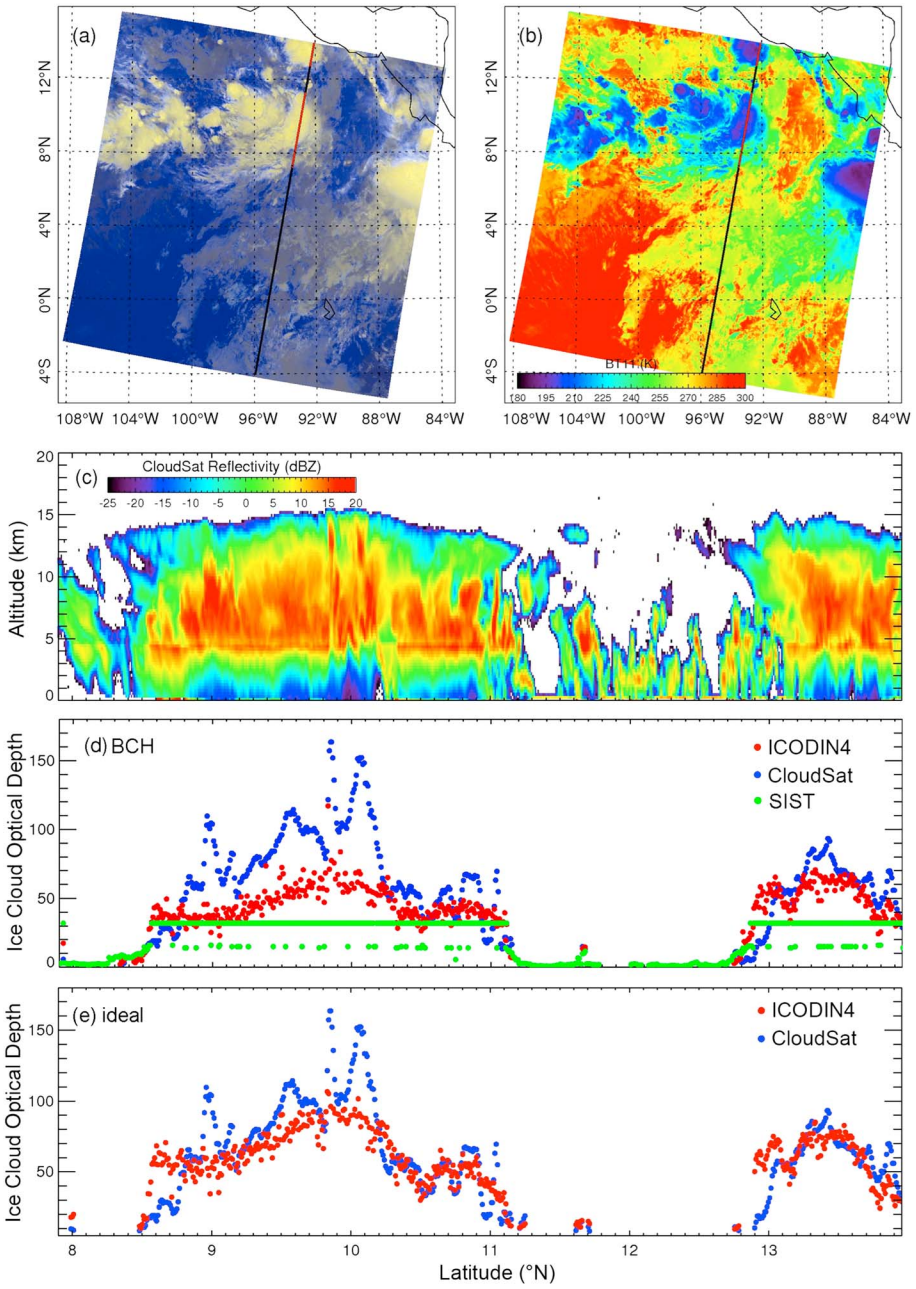

Figure 11. Example of matched Aqua MODIS and CloudSat CPR data and retrievals over eastern tropical Pacific Ocean (108°W–84°W, 4°S–15°N), 0800 UTC, 6 June 2008. (a) MODIS granule RGB (red: inverted BT(11), green: inverted BT(12), and blue: BTD(11–12)) image with overlay of CloudSat ground track as black and red (showing opaque ice clouds) line, (b) MODIS BT(11) with CloudSat ground track, (c) CPR reflectivity along a track segment, and estimated optical thickness from CloudSat (blue) and (d) BCH and (e) ideal ICODIN4 for opaque ice clouds (red).

4.2. Three-Channel Neural Network (ICODIN3a, ICODIN3ab, and ICODIN3ac) Training and Validation

The ICODIN3a (no 3.7 μm channel), the ICODIN3b (no 6.7 μm channel), and ICODIN3c (no 12 μm channel) were trained using only the BCH and validated using the same data sets employed for ICODIN4. The resulting statistics are shown in Table 2 along with those from the BCH and ideal ICODIN4 analyses as well as the SIST retrievals. A total of 537,320 and 1,732,361 matched points were used in ICODIN4 for 2007 and 2008, respectively. The greater number of points in 2008 was possible because the training (2007) was limited by computer memory and the application of the trained algorithm (2008) is not constrained to keep all data in memory. Slightly

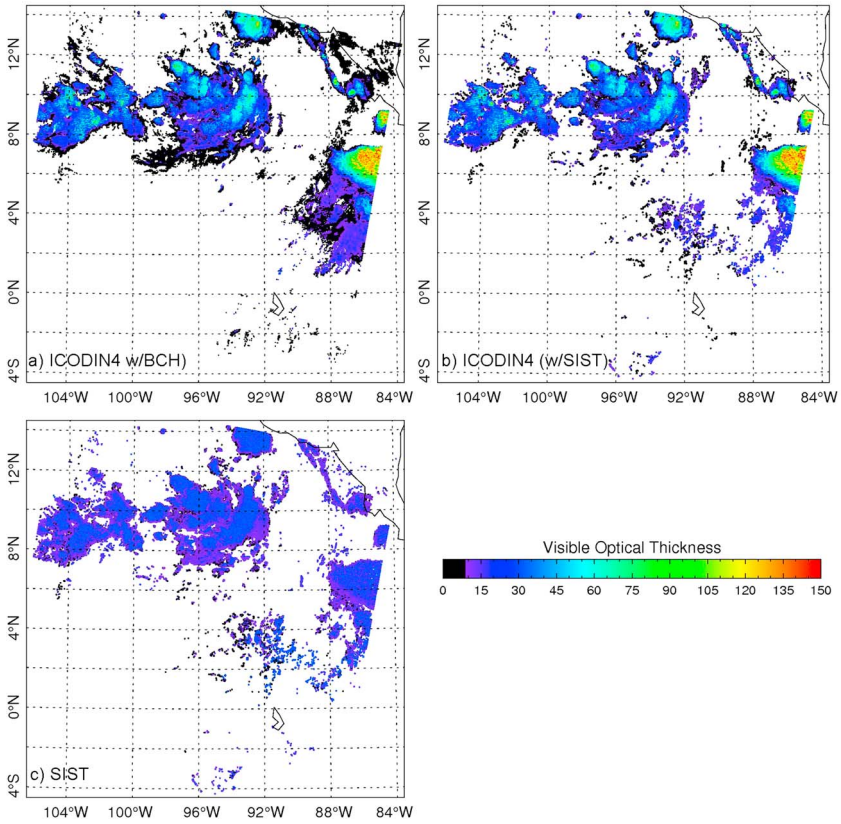

Figure 12. Estimated opaque ice cloud optical thickness for Aqua MODIS granule (see Figures 9a and 9b) at 0800 UTC, 6 June 2008. τ_{CN4} from ICODIN4 (3.7, 6.7, 11.0, and 12.0 μm) using (a) BCH and (b) SIST to identify opaque ice clouds and (c) from CERES Edition 4 SIST retrievals using SIST retrievals or default values for opaque ice clouds.

different numbers of pixels were identified as valid for the ICODIN3 analyses; thus, different mean optical depth values were obtained for each case. Overall, ICODIN4 marginally produces the highest correlation with τ_{CS} and smallest mean SDD, but the results from the various three-channel methods do not differ greatly from the ICODIN4 statistics. The worst neural network performer is ICODIN3a, which lacks the 3.7 μm channel. Its correlation is lowest for the independent retrievals, and the SDD values are greatest overall. Increases in uncertainty occur across the board for the 2008 data. All of the ICODIN methods produce more accurate results than the SIST; the ideal case halves the SIST SDD.

Figure 13 shows the optical depths retrieved using the ICODIN3a, ICODIN3b, and ICODIN3c for the image analyzed in Figure 12. All three methods produce τ patterns similar to those generated by ICODIN4 (Figure 12a), but each finds more extremely high (red) values for the large system on the right than ICODIN4. ICODIN3a (Figure 13b) yields more low values (black) of τ_{CN3a} on the center right and fewer values around 35 or so (dark blue). The ICODIN3b (Figure 13c) more closely resembles the ICODIN4 results overall but tends to run high. ICODIN3c (Figure 13d) is also more like ICODIN4 than ICODIN3b but has fewer extremely high values overall.

The differences and similarities between the three- and four-channel methods are quantified in Figure 14, which shows scatterplots made from the data in Figure 12a matched to the results in Figure 13. Optical depths from ICODIN3a and ICODIN4 (Figure 14a) are highly correlated ($R = 0.91$), but the scatter is quite high with SDD = 9.55, a value larger than that between τ_{CS} and τ_{CN4} (Table 1). The absence of the water vapor channel in ICODIN3b does not seem to make a great amount of difference compared to ICODIN4 as $R = 0.97$ and SDD = 5.53 (Figure 14b). Furthermore, the values at the high end are mostly greater than those from ICODIN4, a tendency that may counteract the shortfall in extremely high values seen in Figure 5. Unlike the nearly linear distribution of points in Figure 14b, the results of ICODIN3c (Figure 14c) yield a clearly nonlinear relationship with an inflection around $\tau_{CN4} \sim 70$ and an overestimating bulge around $\tau_{CS} \sim 25$. Its SDD value is 10% greater than its ICODIN3b counterpart. Although the results in Table 2 all give comparable optical depths relative

Table 2. Correlation and Differences Between ICODIN and CPR Ice Cloud Optical Depths

Retrieval Method	Year	Mean	*R*	Bias	Bias (%)	SDD	SDD (%)
			BCH Opaque Only				
ICODIN43.7, 6.7, 11, and 12 μm	2007	8.85	0.80	−0.07	−0.8	8.73	99
	2008	8.50	0.78	−0.10	−1.2	8.89	105
ICODIN3a6.7, 11, and 12 μm	2007	8.95	0.79	−0.05	−0.6	9.20	103
	2008	8.60	0.75	−0.07	−0.8	9.45	110
ICODIN3b3.7, 11, and 12 μm	2007	8.83	0.79	−0.09	−1.0	8.91	101
	2008	8.51	0.78	−0.10	−1.2	8.94	105
ICODIN3c3.7, 6.7, 11 μm	2007	8.86	0.80	−0.05	−0.6	8.80	99
	2008	8.51	0.77	−0.10	−1.2	9.13	107
SIST	2007	7.40	0.63	−2.42	−24.6	12.2	124.4
	2008	7.16	0.64	−2.19	−23.4	11.6	124.4
			Ideal (*BCH and CloudSat Opaque*)				
Ideal ICODIN4	2007	21.8	0.73	−0.07	−0.3	13.2	61
3.7, 6.7, 11, and 12 μm	2008	21.3	0.71	−0.33	−1.5	13.5	63

to CloudSat, Figure 14 indicates that the absence of the 6.7 μm channel has the least impact on results in contrast to the weights seen in Figure 7. Perhaps, since these data are from the entire image with VZAs up to 67°, they could indicate that the 6.7 μm (3.7 μm) channel is most (least) sensitive to VZA effects.

5. Discussion

The ICODIN approach has skill at retrieving ICOD but appears to have relatively large random uncertainties. Moreover, it only retrieves ICOD and makes no attempt to retrieve the total optical depth, which would include any liquid water in the column. The uncertainties and the impact of ignoring the liquid water are

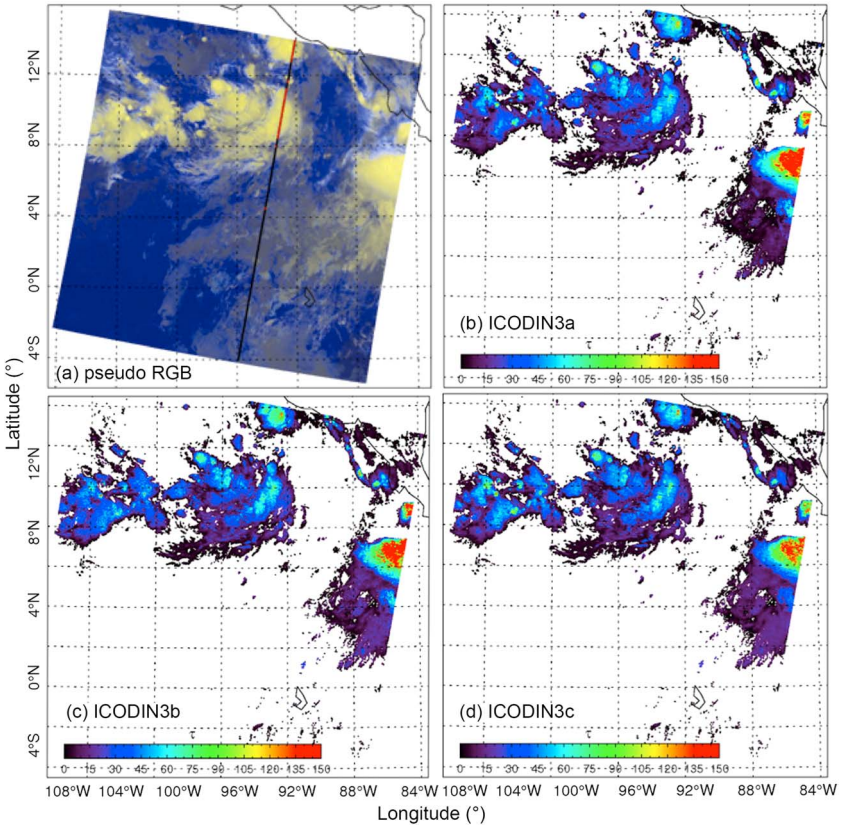

Figure 13. Same as Figure 10 except for (b) τ_{CN3a} from ICODIN3a (6.7, 11.0, and 12.0 μm), (c) τ_{CN3b} from ICODIN3b (3.7, 11.0, and 12.0 μm), and (d) τ_{CN3c} from ICODIN3c (3.7, 6.7, and 11.0). The BCH method was used in all cases to identify opaque ice cloud pixels.

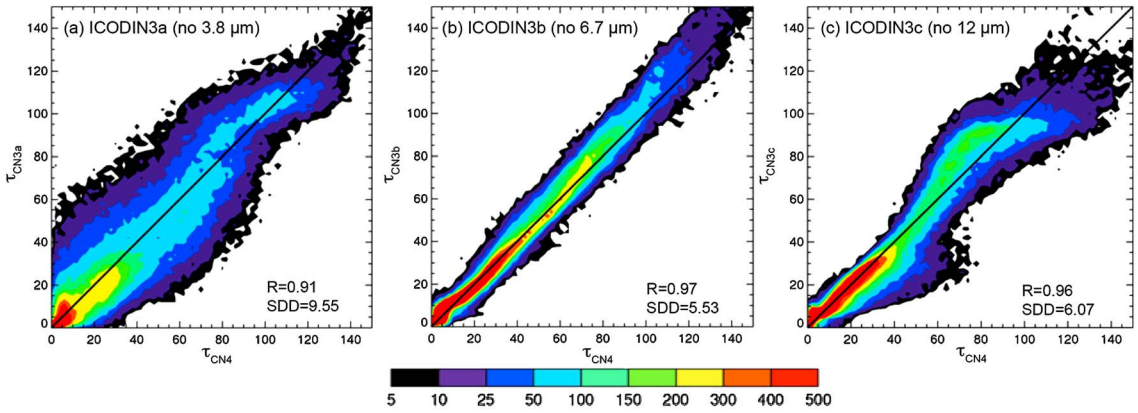

Figure 14. Comparisons of opaque ice cloud optical thickness from three-channel methods with that, τ_{CN4}, from four-channel technique (ICODIN4) for the MODIS granule in Figure 7. (a) τ_{CN3a} from ICODIN3a (6.7, 11.0, and 12.0 μm), (b) τ_{CN3b} from ICODIN3b (3.7, 11.0, and 12.0 μm), and (c) τ_{CN3c} from ICODIN3c (3.7, 6.7, and 11.0).

discussed below. It is beyond the scope of this paper to provide a complete error analysis. Rather, the purpose is to demonstrate the potential of the ICODIN approach and illuminate some of the factors that should be considered when further developing and applying it.

5.1. Uncertainties

As seen in the analysis above, the retrieved ice optical depths are relatively unbiased, on average, but the RMS errors (~SDD) are on the order of 100%. These errors are likely due to limitations in the ICODIN retrievals and to uncertainties in the CloudSat retrievals. As discussed earlier, the sensitivity of the ICODIN channels to changes in optical depth beyond the infrared opaque "limit" is likely due to subtle changes in the cloud top structure and, especially for 6.7 μm, the water vapor in the top levels of the cloud. The relationships among the vertical structure, the ICOD, and the individual channel responses are probably not unique, which would account for some of the scatter and the decreasing ability to detect a dependence on τ at values greater than ~60. For example, the vertical structure at cloud top could be the same for a cloud having $\tau = 70$ or 100 in some cases, but not in others. Because the development of very thick ice clouds is mostly a deep convective phenomenon, τ is also likely to be affected by the vertical profiles of temperature and humidity, the surface temperature, and the stability. In this study, those factors, as well as surface type, were not considered.

At the bottom of the temperature range (BT $<$ 220 K), values of BT(3.7) change by several K/count, drastically reducing the precision of the observation. For extremely cold clouds having very large optical depths, the 3.7 μm channel yields very noisy (and hence uncertain) temperatures that can be either larger or smaller than their 11 μm counterparts. This is illustrated in Figure 15, which shows BT(11) and BTD(3.7–11) for part of a MODIS granule having a convective system over the northeast Pacific at 0925 UTC, 5 July 2012. The BTD (Figure 15b) peaks above 30 K for BT(11) ~ 245 K (Figure 15a). It drops with decreasing BT(11) to 3 or 4 K near 220 K and then varies between -5 and +10 K for BT(11) $<$ 220 K consistent with the inset plots in Figure 2. Striping and noise are evident for the coldest temperatures, where the 3.7 μm signal-to-noise ratio drops dramatically and small calibration differences among the eight MODIS receivers are accentuated. Inaccurate temperatures would reduce the potential for providing a distinct optical depth signal that could be exploited by the ICODIN. The apparent capability of retrieving larger optical depths without the 6.7 μm channel (Figure 14b), however, suggests that this is not a large issue. On the other hand, the three-channel combination lacking the 3.7 μm data (Figure 14c) has the fewest values of $\tau > 100$. This suggests that the 3.7 μm channel is most sensitive to τ, so that having smaller errors in BT(3.7) at the low end of the range (180–200 K) could lead to the retrieval of more values of $\tau > 70$. This is consistent with the detailed radiative transfer calculations in *Minnis et al*. [2012] that show BTDs using BT(3.7) continue to decrease toward zero for $\tau > 100$. It, however, is not consistent with relative importance of the channels seen in Figure 7.

Because the thermal radiation channels used here are sensitive to the vertical profiles of IWC and particle size, the measured radiances that serve as input to the ICODIN can be affected by subtle variations in the vertical profiles of those parameters, especially near cloud top. The CloudSat retrievals used to train the ICODIN,

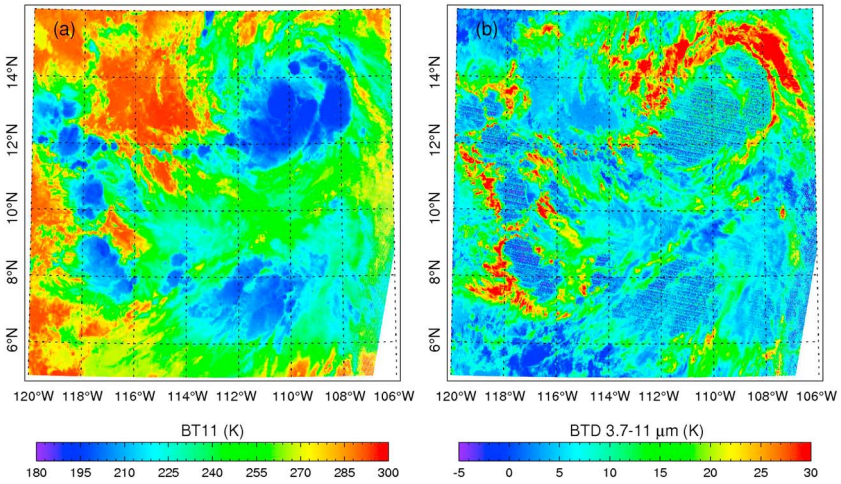

Figure 15. Aqua MODIS image at night over the eastern Pacific at 0925 UTC, 5 July 2012, (a) BT(11) and (b) BTD(3.7–11).

however, are based on retrievals of IWC that can be highly uncertain. In addition to being biased high by ~25% relative to in situ measurements, the uncertainty in the individual retrievals often exceeds 100% [*Austin et al.*, 2009], especially for lower temperatures, IWC < 0.1 g m^{-3}, and for clouds having $\tau < 15$. Thus, some of the sensitivity to variations in IWC that can affect the passive radiances is not likely being faithfully represented in the training set's output data. Thus, uncertainties of 100% in the ICODIN retrievals are not surprising.

The goal of developing the neural network method here was to retrieve optical depths for opaque clouds as defined by the BCH. Yet a large fraction of the ice clouds identified as opaque by the BCH or the SIST were classified as semitransparent by the CloudSat analysis. Those retrievals are included in the statistics in Table 2. Computing the difference statistics only for clouds classified as opaque by the ICODIN or by CloudSat provides a better representation of how well the original goal was met. Tables 3 and 4 list the difference statistics for those MODIS pixels having $\tau_{CS} \geq 8$ and $\tau_{CN} \geq 8$, respectively. These data comprise a subset of the entire data set used for Table 2. Removing the smaller CloudSat optical depths (Table 3) yields lower correlations and a significant bias in the ICODIN results, as expected from Figures 5 and 6. The −20% bias in the mean τ_{CN} for $\tau_{CS} \geq 8$ is accompanied by an ~20% decrease in SDD indicating that many of the largest relative uncertainties in Table 2 were due to clouds having lower optical depths. In Table 4, the correlations are similar to those in Table 3, but the biases are eliminated and the SDDs drop by another few percent. Thus, when the ICODIN (not the BCH) classifies the cloud as opaque, it will, on average, have the same ICOD as the CloudSat retrieval.

The original goal, then, is partially met. Of the total number of pixels originally identified as opaque, ~67% are semitransparent and ~33% are opaque, according to ICODIN4. The pixels having $\tau_{CN} < 8$ and $\tau_{CS} \geq 8$ comprise ~7% of the total fraction of pixels. This identification agreement or lack thereof is summarized in Table 5, which breaks down the various classifications for the ICODIN4 and CloudSat results by percent of the total number of pixels. For reference, of the 6.94 (7.44) million matched pixels containing some ice according to CloudSat during 2007 (2008), 0.77 (0.80) million have $\tau_{CS} \geq 8$. Both ICODIN4 and CloudSat agree on the classification ~84% of the time. The disagreement is nearly balanced with ICODIN4, on the whole, producing 1–2% more opaque clouds than CloudSat. The near balance is also seen in the optical depths. For those pixels having $\tau_{CN} < 8$ and $\tau_{CS} \geq 8$, the average $\tau_{CN} = 4.7$, while the mean τ_{CN} is 12.5 for those having $\tau_{CN} \geq 8$ and $\tau_{CS} < 8$. The misclassification of ~68% of the pixels as opaque by BCH and the accuracy of the ideal method suggest the need to develop a more accurate opaque ice cloud screening technique. However, the correct (according to CloudSat) reclassification of ~60% of the BCH opaque pixels as semitransparent indicates that ICODIN4 can also serve as an effective screening method for many semitransparent ice clouds.

If the SIST is used to select opaque pixels, the agreement is also ~84% overall, but ~51% of the pixels selected by the SIST are truly opaque according to CloudSat. The reduced total number of pixels, however, belies the notion that the SIST is better at selecting opaque clouds. For reference, of the 6.94 (7.44) million matched

Table 3. Same as Table 2 Except for All Pixels With $\tau_{CS} \geq 8$

Method	Year	Mean	*R*	Bias	Bias (%)	SDD	SDD (%)
ICODIN43.7, 6.7, 11, and 12 μm	2007	18.6	0.72	−3.7	−19.9	14.2	76.3
	2008	18.1	0.69	−3.95	−21.8	14.7	81.2
ICODIN3a6.7, 11, and 12 μm	2007	18.0	0.72	−4.5	−25.0	14.7	81.7
	2008	17.4	0.68	−4.8	−27.5	15.3	87.9
ICODIN3b3.7, 11, and 12 μm	2007	18.3	0.71	−4.0	−21.9	14.4	78.7
	2008	17.9	0.69	−4.1	−22.9	14.7	82.1
ICODIN3c3.7, 6.7, and 11 μm	2007	18.5	0.72	−3.8	−20.5	14.3	77.3
	2008	18.0	0.77	−4.1	−22.8	15.1	83.9
SIST	2007	12.6	0.53	−9.84	−43.8	19.6	87.2
	2008	12.6	0.54	−9.61	−43.3	19.1	86.1

pixels containing some ice according to CloudSat during 2007 (2008), 0.77 (0.80) million have $\tau_{CS} \geq 8$. Thus, the SIST detects only 37% of the total number of CloudSat opaque pixels compared to 67% for the BCH. BCH maximizes the opaque cloud detection at the expense of increased false detections. The SIST reduces the number of false detections but detects fewer opaque clouds.

5.2. Comparisons With Other Retrievals

Currently, thick cloud optical depths are mostly retrieved using reflected solar radiation measurements. However, such retrievals yield the total cloud optical depth and not the separate contributions from ice and water hydrometeors that together often comprise the observed cloud. Optically thick ice clouds are commonly part of convective systems that are vertically contiguous with liquid water clouds or that have anvils overlying low clouds or that are part of a baroclinic system with layers of liquid clouds below the ice layers. Despite these potential differences, it is necessary to compare the ICODIN retrievals with their reflectance-based counterparts to determine how they are related since the goal is to eventually develop a total visible optical depth τ_V at night that matches the daytime retrievals as closely as possible. To begin that process, two comparisons are made here.

Figure 16 shows the results for a nocturnal case from an Aqua MODIS image over the tropical eastern Pacific at 0925 UTC, 5 July 2012. The pseudo-RGB image (Figure 16a) reveals areas of deep convection in various stages of development and dissipation. This case was selected because the Aqua and SNPP overpasses match closely so that VIIRS and MODIS view essentially the same area at the same time. The optical depths from MODIS using ICODIN4 are shown in Figures 16b and 16c using the BCH and SIST, respectively, to select thick ice clouds. The results based on SIST are the same as those using the BCH criteria except that the SIST appears to identify some thin cirrus over low clouds as being opaque (~5.5°N, 116°W). If the SIST alone is used to determine the optical depths (Figure 16d), much of the selected cloud area is set to the default value of 32. These results can be compared with the DNB retrievals from VIIRS in Figure 16e, which shows many clouds having $\tau_{DNB} > 120$. In most instances, $\tau_{DNB} > \tau_{CN4}$. As noted above, this result is not surprising given that a significant portion of the cloud column is likely in liquid form and ICODIN typically underestimates the ICOD when it exceeds 70. This can be seen in the light blue areas in Figure 16b/16c, which have values of 60–70, while the DNB optical depths are mostly red with $\tau_{DNB} > 120$.

Table 4. Same as Table 2 Except for All Pixels With $\tau_{CN} \geq 8$

Method	Year	Mean	*R*	Bias	Bias (%)	SDD	SDD (%)
ICODIN43.7, 6.7, 11, and 12 μm	2007	19.7	0.73	−0.05	−0.2	14.0	71.1
	2008	19.5	0.69	−0.04	−0.2	14.5	74.3
ICODIN3a6.7, 11, and 12 μm	2007	19.3	0.71	−0.04	−0.2	14.5	75.1
	2008	19.0	0.67	0.08	0.4	15.2	80.0
ICODIN3b3.7, 11, and 12 μm	2007	19.6	0.72	0.02	0.1	14.2	72.4
	2008	19.5	0.69	0.09	0.5	14.5	74.3
ICODIN3c3.7, 6.7, and 11 μm	2007	20.1	0.72	0.00	0.0	14.3	71.1
	2008	19.9	0.66	−0.05	−0.3	15.2	76.4

Table 5. Frequency (%) of Cloud Thickness Category, CODIN4 System Versus CloudSat[a]

Method	BCH				SIST			
Year	2007		2008		2007		2008	
# samples	1.612×10^6		$1.7\ 32 \times 10^6$		0.555×10^6		0.573×10^6	
Category	$\tau_{CS} < 8$	$\tau_{Cs} \geq 8$	$\tau_{CS} < 8$	$\tau_{CS} \geq 8$	$\tau_{CS} < 8$	$\tau_{CS} \geq 8$	$\tau_{CS} < 8$	$\tau_{CS} \geq 8$
$\tau_{CN4} < 8$	59.0	7.0	60.4	7.2	35.4	2.9	35.8	2.9
$\tau_{CN4} \geq 8$	8.8	25.2	8.6	23.8	13.1	48.6	13.3	48.0
Original opaque	67.8	32.2	69.0	31.0	48.5	51.5	49.1	50.9

[a]Original opaque indicates the fraction of pixels classified by BCH or SIST as opaque ice.

Similarly, Figure 17 gives an example of applying ICODIN3a to a daytime image, in this case, from Aqua MODIS data taken over the tropical western Pacific at 0235 UTC, 1 February 2007. ICODIN3a is used in the daytime because it does not use the 3.7 μm temperatures, which include reflected solar energy. The pseudo-RGB and BT(11) images in Figures 17a and 17b, respectively, indicate areas of very deep convection (dark blue in Figure 17b) with low clouds scattered among the ice cloud areas. The ICODIN3a retrievals were performed using the BCH (Figure 17c) and VISST (Figure 17d) criteria for optically thick ice clouds. During daytime, the VISST retrieves optical depth directly from the 0.65 μm reflectance, so the opacity should be less uncertain than when using SIST. The ICODIN3a retrievals can be compared to the VISST optical depths in Figure 17e. As in the DNB case, the optical depths from the neural network approach are generally less than their VISST counterparts; however, there appear to be more instances where the $\tau_{CN3a} > \tau_{VISST}$ than for the DNB case in Figure 16. This could be expected to happen based on the noisier ICODIN3a retrievals shown in Figure 14, which have considerable scatter relative to their ICODIN4 counterparts and should, therefore, overestimate or underestimate τ_{CS} by greater amounts than ICODIN4.

Daytime retrievals of τ or IWP for thick ice clouds, similar to those in Figures 16 and 17, generally assume that the cloud is entirely ice and the effective particle size for the entire cloud is the same as the retrieved value, even though it often represents only the top portion of the cloud column. As shown by *Minnis et al*. [2007] and others, the true total optical depth retrieved with that assumption will typically be underestimated by τ_{VISST} or τ_{DNB}, but that is a problem addressed elsewhere [*Smith*, 2014]. The parameter, τ_{VISST}, retrieved at solar wavelengths uses the single-phase assumption. Thus, to achieve parity between τ_{CS} or τ_{CN} and τ_{VISST}, it is necessary to find some means for estimating τ_V from the ice optical depth.

For purposes of demonstration, τ_V is estimated here for the two images in Figures 16b and 17c using one of potentially many approaches. *Smith* [2014] developed a method for estimating vertical profiles of cloud water content (CWC) based on MODIS retrievals of T_c, τ_{VISST}, and IWP_{VISST} matched to CloudSat CWC. The technique also yielded a parameterization of the IWP_{CS} as a function of IWP_{VISST}, which is typically underestimated for optically thick ice clouds because of larger particle sizes in the interior of the cloud than at cloud top. *Smith* [2014] applied the parameterization, which assumes that liquid water comprises a portion of the ice cloud whenever $\tau_{VISST} > 10$, to more than 250,000 GOES pixels and tabulated the resulting mean values of τ_{VISST} and IWP_{CS} for six intervals of τ_{VISST}. Assuming equivalence of τ_{CS} and τ_{CN}, and that r_e of the ice portion of the cloud increases with IWP_{CS} from 30 to 80 μm, the estimated value of τ_{CN} was computed as the product, $1.5 \times IWP_{CS}/r_e$. With those assumptions, the resulting relationship is

$$\tau_V = 0.976 \times \tau_{CN} + 0.0115 \times \tau_{CN}^2. \quad (4)$$

Equation (4) was applied to values of $\tau_{CN} > 10$ from BCH-ICODIN for the images in Figures 16 and 17. The results are compared in Figure 18 to those from VISST applied during the night using the VIIRS DNB channel (Figures 16e and 18a) and during the day using the MODIS visible channel (Figures 17d and 18c). The nocturnal values of τ_V (Figure 18b) appear to be much closer to their DNB counterparts (Figure 18a) than the τ_{CN4} results (Figure 16b). There appears to be excellent agreement for the contiguous red areas in the main cloud mass (upper right). However, τ_{DNB} for the brightest clouds in the other systems remains underestimated by τ_V. This is likely due to the large optical depth limitations discussed earlier, although the DNB retrievals could be biased. A 5% uncertainty in the illumination can result in large uncertainties in the retrieved optical depth for optically thick clouds. Nevertheless, this initial result is encouraging for providing a reasonable total

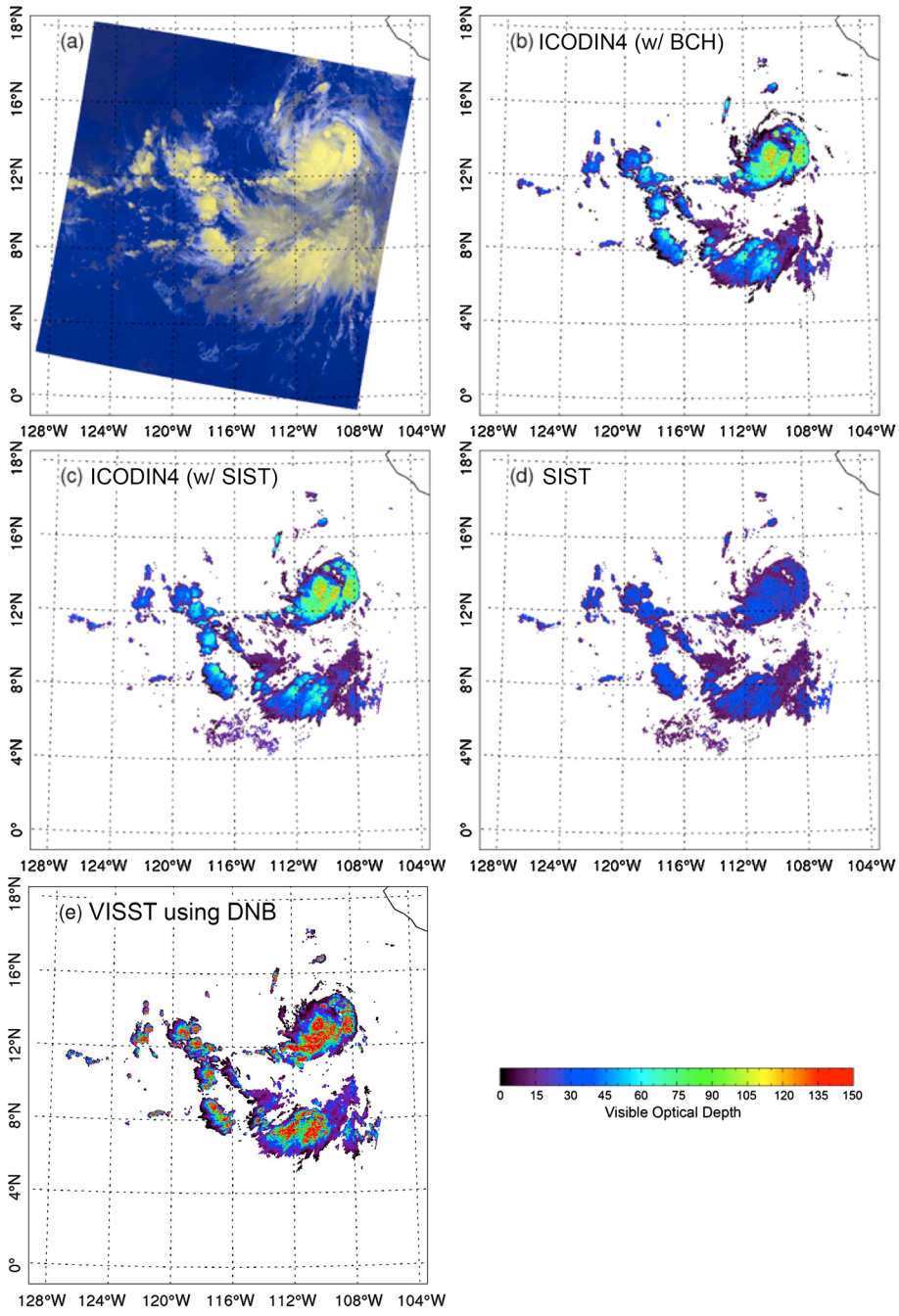

Figure 16. Opaque ice cloud optical depths estimated using three methods at night over the eastern Pacific at 0925 UTC, 5 July 2012. (a) Aqua MODIS RGB (red: inverted BT(11), green: inverted BT(12), and blue: BTD(3.7–11)); τ_{CN4} estimated from ICODIN4 applied to Aqua MODIS data with (b) BCH and (c) SIST selection of opaque clouds, (d) τ estimated from SIST method, and (e) opaque ice cloud τ estimated from DNB retrieval applied to matching SNPP VIIRS data.

optical depth estimate for these thick ice clouds at night. With proper assumptions about the effective radii of the ice and water portions of those clouds, a more realistic estimate of CWP could also be made.

The potential for estimating τ_V during daytime with infrared data only is similar. It is clear in Figure 18d that τ_V still generally underestimates τ_{VISST} (Figure 18c). Even though τ_V is considerably closer to τ_{VISST} than τ_{CN3a} (Figure 17c), it tends to produce some maxima that are not seen in the VISST retrievals. Again, this is due to the noisy retrieval discussed earlier. Ideally, having an accurate independent measurement of the ice optical depth during daytime would allow the retrieval of the liquid cloud optical depth underneath the ice cloud

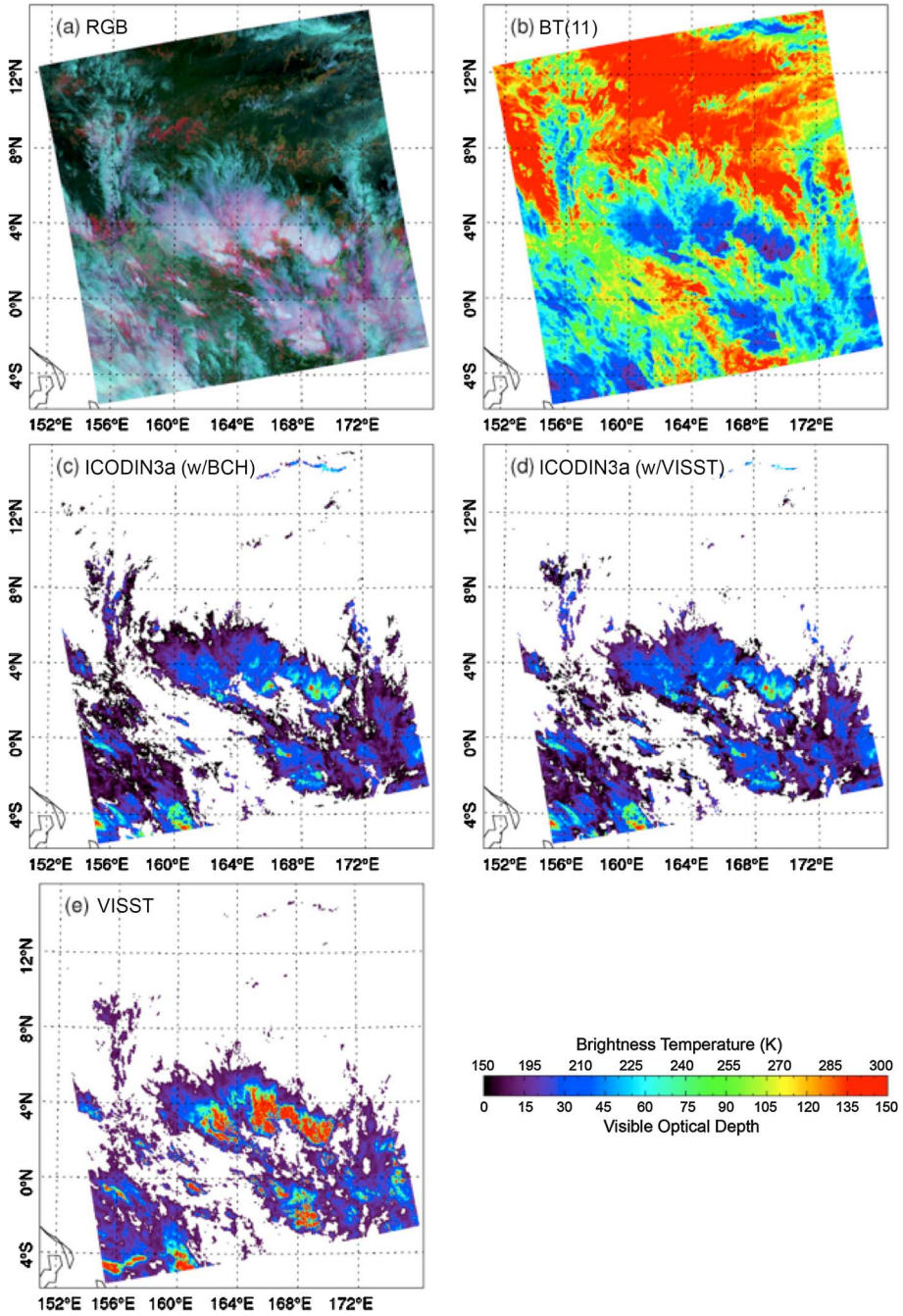

Figure 17. Comparison of cloud optical thicknesses estimated over western Pacific from daytime Aqua MODIS data taken at 0235 UTC, 1 February 2007. (a) RGB (red: 0.64 μm reflectance, green: BTD(3.7–11), and blue: BT(11)) image. (b) BT(11). τ_{CN3a} from ICODIN3a using (c) BCH and (d) VISST to select opaque ice clouds. (e) Total cloud τ estimated using VISST.

and together yield a more accurate total optical depth and a better estimate of the CWP. The results in CODIN3a suggest that its accuracy is currently insufficient for that application. It should be noted that this example case uses a crude approximation to estimate τ_V simply for demonstration, so any final conclusion about the efficacy of using ICODIN3a is unwarranted. Perhaps, with further refinement it could be used to improve daytime retrievals of multiphase and thick ice-over-water multilayered clouds using a method similar to that employed by *Minnis et al*. [2007] to retrieve IWP from combined microwave LWP and imager retrievals of τ_{VISST}.

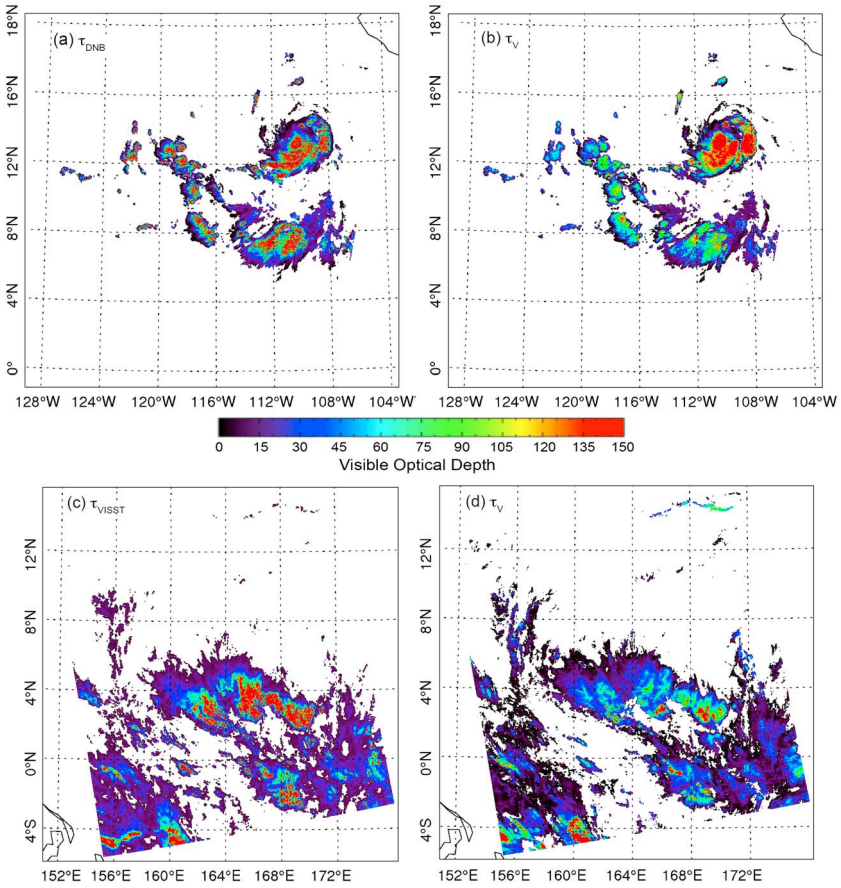

Figure 18. Cloud optical depths for images in (a and b) Figure 16a and (c and d) Figure 17a. Optical depths derived from VIIRS DNB channel (Figure 18a) , τ_{CN4} and equation (3) (Figure 18b), MODIS visible channel (Figure 18c), and τ_{CN3a} and equation (3) (Figure 18d).

6. Conclusions

A neural network approach, ICODIN, using four combinations of thermal and shortwave infrared wavebands has been developed to estimate opaque ice cloud optical depths at night, a quantity heretofore ignored in passive infrared remote sensing due to the blackbody limit of infrared emission. Clouds, especially those composed of ice crystals, are not true blackbodies but have detailed vertical structures of ice water content, particle size and shape, water vapor, and temperature that can affect the emitted radiances. Subtle changes in those components related to the overall depth of the cloud as well as the radiating temperature of the cloud top can potentially provide some information about the ICOD. This potential is the physical basis for the application of the neural network to this problem. Training of the ICODIN used only 2 months of CloudSat data taken over the entire Earth. Even with no distinction between air masses, surface types and temperatures, and cloud types, the ICODIN yields ice cloud optical depths that are highly correlated, explaining 64% of the variance, with those from the CloudSat radar-only algorithm and are unbiased, on average.

Application of the ICODIN requires initial screening of the data to identify opaque ice clouds, which are those assumed to have optical depths greater than or equal to 8. The two screening techniques used here, the BCH and SIST, greatly overestimate the frequency of opaque ice clouds, but the ICODIN successfully accounts for the semitransparent cloud pixels by assigning them more appropriate values of τ. Using four channels (ICODIN4) marginally produces the smallest uncertainties relative to CloudSat, but in terms of overall errors, three- or four-channel methods are quite comparable. The complement lacking the 3.7 μm channel yields the largest uncertainties, while the combination of 3.7, 11, and 12 μm (ICODIN3b) appears to be the most promising three-channel complement and most sensitive to ICOD. When the ICODIN4 trained with the BCH scene classification determines a cloud to have $\tau > 8$, the result is, on average, unbiased with respect to CloudSat

and has a relative standard error of ~72%. The relative error increases to 100% if clouds of all ICODs are included. If ICODIN4 is trained using only those pixels having both $\tau_{CS} > 8$ and classified as opaque by BCH, the results are unbiased and the relative error drops to ~62%. This finding is a strong motivation for finding a technique that reliably discriminates between opaque and nonopaque ice clouds.

The training of the ICODIN here has relied on the CloudSat 2B-CWC-RO product, which is known to have relatively large uncertainties that undoubtedly contribute to some of the error in the ICODIN retrievals. Training with other IWC products [e.g., *Deng et al*., 2010; *Delanoë and Hogan*, 2010] that include CALIPSO will likely yield similar results in a relative sense because they are all closely correlated with the same in situ measurements [*Deng et al*., 2013]. Because CloudSat and CALIPSO are experimental satellites, their retrieval algorithms are periodically updated to improve the accuracy of the various parameters. Future research into neural networks for opaque cloud retrievals at night should explore the use of the alternative IWC retrievals as well as revisions of the 2B-CWC-RO product. Additionally, the radar-retrieved values of r_e should be analyzed to develop a means for computing IWP from τ_{CN} with the goal of estimating CWP for the subject cloud systems.

The analysis presented here has only begun the exploration of the ICODIN's potential. Reduction of uncertainties in the ICODIN may be possible by using a larger training data set that incorporates data from all months of the year and possibly from additional years. The influence of the air mass, which may also impact the accuracy, could be taken into account by introducing additional input parameters such as the surface type and numerical weather analyses of surface temperature and temperature and humidity at selected levels. In the absence of a sensor having high precision for BT(3.7) < 220 K, it may be helpful to provide the algorithm with some indicator of the quality of the BT(3.7) value in order to downplay its influence at very low temperatures. An indicator of cloud type, such as stratiform or convective, might also be valuable as an input. With the implementation of these additional suggestions, it might be possible to significantly increase the technique's accuracy.

Only near-nadir measurements from MODIS were used in the development of the ICODIN. Thus, application of the method to satellite imager data will require understanding the dependence of the technique on VZA and may require training with other data sets, such as GOES or VIIRS, which provide a wide range of VZA views when matched with CloudSat. The examples shown here suggest that the VZA effect may be relatively small. The use of the technique for other imagers such as VIIRS may require some means to account for differences in the spectral response functions such as spectral band adjustment factors that are based on hyperspectral data [e.g., *Scarino et al*., 2016].

This study has definitively shown that the optical depth of ice clouds can be estimated with reasonable accuracy for clouds that are thicker than the "blackbody limit." While much additional analysis remains to be done, the development of the ICODIN approach opens up the potential for more accurate 24 h monitoring of clouds and for providing forecast models with estimates of cloud water path at all times of the diurnal cycle.

Acknowledgments
This research is supported by the NASA Modeling, Analysis, and Prediction Program and the NASA CERES Project. Thanks to the three anonymous reviewers who helped make this a better manuscript. The data used in this study can be accessed at NASA Langley Research Center upon request.

References

Austin, R. (2007), Level 2B Radar-only Cloud Water Content (2B-CWC-RO) process description document, Algorithm Theoretical Basis Document, CloudSat Project, Ver. 5.1, 21 October, 24 pp. [Available at ftp://ftp.cira.colostate.edu/ftp/CloudSat/Docs/2B-CWC-RO_PDICD.P_R04.20071021.pdf.]

Austin, R. T., A. J. Heymsfield, and G. L. Stephens (2009), Retrieval of ice cloud microphysical parameters using the CloudSat millimeter-wave radar and temperature, *J. Geophys. Res.*, *114*, D00A23, doi:10.1029/2008JD010049.

Baum, B. A., P. F. Soulen, K. I. Strabala, M. D. King, S. A. Ackerman, W. P. Menzel, and P. Yang (2000), Remote sensing of cloud properties using MODIS airborne simulator imagery during SUCCESS: II. Cloud thermodynamic phase, *J. Geophys. Res.*, *105*, 11,781–11,792, doi:10.1029/1999JD901090.

Chen, Y., H. Wang, J. Min, X.-Y. Huang, P. Minnis, R. Zhang, J. Haggerty, and R. Palikonda (2015), Variational assimilation of cloud liquid/ice water path, *J. Appl. Meteorol. Climatol.*, *54*, 1809–1825, doi:10.1175/JAMC-D-14-0243.1.

Choi, Y. S., C.-H. Ho, M.-H. Ahn, and Y. M. Kim (2007), An exploratory study of cloud remote sensing capabilities of the Communication, Ocean and Meteorogical Satellite (COMS) imagery, *Intl. J. Remote Sens.*, *28*, 4715–4732, doi:10.1080/01431160701264235.

Delanoë, J., and R. J. Hogan (2010), Combined CloudSat-CALIPSO-MODIS retrievals of the properties of ice clouds, *J. Geophys. Res.*, *115*, D00H29, doi:10.1029/2009JD012346.

Deng, M., G. G. Mace, Z. Wang, and H. Okamoto (2010), Tropical composition, cloud and climate coupling experiment validation for cirrus cloud profiling retrieval using CloudSat radar and CALIPSO lidar, *J. Geophys. Res.*, *115*, D00J15, doi:10.1029/2009JD013104.

Deng, M., G. G. Mace, Z. Wang, and R. P. Lawson (2013), Evaluation of several A-Train ice cloud retrieval products with in situ measurements collected during the SPARTICUS campaign, *J. Appl. Meteorol. Climatol.*, *52*, 1014–1030, doi:10.1175/JAMC-D-12-054.1.

Fridlind, A. M., et al. (2012), A comparison of TWP-ICE observational data with cloud-resolving model results, *J. Geophys. Res.*, *117*, D05204, doi:10.1029/2011JD016595.

Garson, G. D. (1991), Interpreting neural network weights, *Artif. Intell. Expert*, *6*, 47–51.

Heidinger, A. K. (2003), Rapid daytime estimation of cloud properties over a large area from radiance distributions, *J. Atmos. Oceanic Technol.*, *20*, 1237–1250.

Hillger, D., et al. (2013), First-light imagery from Suomi NPP VIIRS, *Bull. Am. Meteorol. Soc.*, *94*, 1019–1029.
Hong, G., P. Yang, A. K. Heidinger, M. J. Pavolonis, B. A. Baum, and S. E. Platnick (2010a), Detecting opaque and nonopaque tropical upper tropospheric ice clouds: A trispectral technique based on the MODIS 8–12 μm window bands, *J. Geophys. Res.*, *115*, D20214, doi:10.1029/2010JD014004.
Hong, G., P. Minnis, J. K. Ayers, C. R. Yost, and W. L. Smith Jr. (2010b), Nighttime retrievals of cloud properties from infrared radiances at 3.7, 6.7, 11.0, and 12.0 μm, paper P1.10 at AMS 17th Conference on Satellite Meteorology & Oceanography, Annapolis, Md., Sept. 27–30. [Available online at http://www-pm.larc.nasa.gov/site/doc-library/259-AMS_2010_17th.pdf.]
Hong, G., P. Minnis, W. L. Smith Jr., S. Sun-Mack, J. K. Ayers, C. R. Yost, and Y. Chen (2012), Non-opaque and opaque ice cloud properties from infrared radiances at 3.7, 6.7, 11.0, and 12.0 μm, paper IRS2012-491-2 presented at 2012 International Radiation Symposium, Berlin, Germany, 6–10 Aug. [Available online at http://www-pm.larc.nasa.gov/site/doc-library/258-IRS2012_Hong.pdf.]
Huang, H.-L., P. Yang, H. Wei, B. A. Baum, Y. X. Hu, P. Atonelli, and S. A. Ackerman (2004), Inference of ice cloud properties from high spectral resolution infrared observations, *IEEE Trans. Geosci. Remote Sens.*, *42*, 842–852.
Im, E., S. L. Durden, and C. Wu (2005), Cloud profiling radar for the CloudSat mission, *IEEE Trans. Aerosp. Electron. Syst.*, *20*, 15–18, doi:10.1109/MAES.2005.1581095.
Inoue, T. (1985), On the temperature and effective emissivity determination of semi-transparent cirrus clouds by bispectral measurements in the 10 micron window region, *J. Meteorol. Soc. Jpn.*, *63*, 88–99.
Jones, T. A., D. J. Stensrud, P. Minnis, and R. Palikonda (2013), Evaluation of a forward operator to assimilate cloud water path into WRF-DART, *Mon. Weather Rev.*, *141*, 2272–2289, doi:10.1175/MWR-D-12-00238.1.
Jones, T. A., D. J. Stensrud, L. Wicker, P. Minnis, and R. Palikonda (2015), Simultaneous radar and satellite data storm-scale assimilation using an ensemble Kalman filter approach for 24 May 2011, *Mon. Weather Rev.*, *143*, 165–194, doi:10.1175/MWR-D-14-00180.1.
Jones, T. A., K. Knopfmeier, D. Wheatley, G. Creager, P. Minnis, and R. Palikonda (2016), Storm-scale data assimilation and ensemble forecasting with the NSSL Experimental Warn-on Forecast. Part 2: Combined radar and satellite data experiments, *Weather Forecast.*, *31*, 297–327, doi:10.1175/WAF-D-15-0107.1.
Karayiannis, N. B., and A. N. Venetsanopoulos (1993), Efficient learning algorithms for neural networks (ELEANNE), *IEEE Trans. Syst. Man Cybern.*, *23*, 1372–1383.
Kato, S., S. Sun-Mack, W. F. Miller, F. G. Rose, Y. Chen, P. Minnis, and B. A. Wielicki (2010), Relationships among cloud occurrence frequency, overlap, and effective thickness derived from CALIPSO and CloudSat merged cloud vertical profiles, *J. Geophys. Res.*, *115*, D00H28, doi:10.1029/2009JD012277.
Kato, S., et al. (2011), Improvements of top-of-atmosphere and surface irradiances with CALIPSO, CloudSat, and MODIS-derived cloud and aerosol properties, *J. Geophys. Res.*, *116*, D19209, doi:10.1029/2011JD016050.
King, M. D., W. P. Menzel, Y. J. Kaufman, D. Tanre, B.-C. Gao, S. Platnick, S. A. Ackerman, L. A. Remer, R. Pincus, and P. A. Hubanks (2003), Cloud and aerosol properties, precipitable water, and profiles of temperature and water vapor from MODIS, *IEEE Trans. Geosci. Remote Sens.*, *41*, 442–458.
Kox, S., L. Bugliaro, and A. Ostler (2014), Retrieval of cloud optical thickness and top altitude from geostationary remote sensing, *Atmos. Meas. Tech.*, *7*, 3233–3246, doi:10.5194/amt-7-3233-2014.
Lin, X., and J. Coakley Jr. (1993), Retrieval of properties for semitransparent clouds from multispectral infrared imagery data, *J. Geophys. Res.*, *98*, 18,501–18,514.
Liou, K.-N., S. C. Ou, Y. Takano, F. P. J. Valero, and T. P. Ackerman (1990), Remote sounding of the tropical cirrus cloud temperature and optical depth using 6.5 and 10.5 μm radiometers during STEP, *J. Appl. Meteorol.*, *29*, 716–726.
McGill, M. J., L. Li, W. D. Hart, G. M. Heymsfield, D. L. Hlavka, P. E. Racette, L. Tian, M. A. Vaughan, and D. M. Winker (2004), Combined lidar-radar remote sensing: Initial results from CRYSTAL-FACE, *J. Geophys. Res.*, *109*, D07203, doi:10.1029/2003JD004030.
Menzel, W. P., R. A. Frey, B. A. Baum, and H. Zhang (2006), MODIS cloud top properties and cloud phase algorithm theoretical basis document. [Available at http://modis.gsfc.nasa.gov/data/atbd/atbd_mod04.pdf.]
Miller, S. D., and R. E. Turner (2009), A dynamic lunar spectral irradiance data set for NPOESS/VIIRS day/night band nighttime environmental applications, *IEEE Trans. Geosci. Remote Sens.*, *47*, 2316–2329.
Minnis, P., J. Huang, B. Lin, Y. Yi, R. F. Arduini, T.-F. Fan, J. K. Ayers, and G. G. Mace (2007), Ice cloud properties in ice-over-water cloud systems using TRMM VIRS and TMI data, *J. Geophys. Res.*, *112*, D06206, doi:10.1029/2006JD007626.
Minnis, P., et al. (2008a), Near-real time cloud retrievals from operational and research meteorological satellites, paper 7107-2 presented at Proceedings of SPIE Europe Remote Sensing 2008, Cardiff, Wales, U. K., 15–18 Sept. [Available online at http://www-pm.larc.nasa.gov/site/doc-library/99-Minnis.etal.SPIE.abs.08.pdf.]
Minnis, P., C. R. Yost, S. Sun-Mack, and Y. Chen (2008b), Estimating the physical top altitude of optically thick ice clouds from thermal infrared satellite observations using CALIPSO data, *Geophys. Res. Lett.*, *35*, L12801, doi:10.1029/2008GL033947.
Minnis, P., G. Hong, W. L. Smith Jr., and P. W. Heck (2010a), Cloud optical depths at night: Going beyond the infrared blackbody limits, paper presented at 2010 NOAA STAR AWG/RRR-Review, Madison, Wis., June 7–11. [Available online at http://www-pm.larc.nasa.gov/site/doc-library/256-Minnis.poster.AWG.10.pdf.]
Minnis, P., et al. (2010b), CERES Edition 3 cloud retrievals, paper 5.4 presented at AMS 13th Conference on Atmospheric Radiation, Portland, Oreg., June 27–July 2. [Available online at https://ams.confex.com/ams/pdfpapers/171366.pdf.]
Minnis, P., G. Hong, J. K. Ayers, W. L. Smith Jr., S. Sun-Mack, C. R. Yost, Y. Chen, and P. W. Heck (2011a), Enhanced nighttime cloud retrievals, paper presented at 2011 NOAA STAR GOES-R AWG Annual Review, Fort Collins, Colo., June 14–16. [Available online at http://www-pm.larc.nasa.gov/site/doc-library/257-Minnis.poster.AWG.11.pdf.]
Minnis, P., et al. (2011b), CERES edition-2 cloud property retrievals using TRMM VIRS and Terra and Aqua MODIS data. Part I: Algorithms, *IEEE Trans. Geosci. Remote Sens.*, *49*, 4374–4400.
Minnis, P., et al. (2012), Simulations of infrared radiances over a deep convective cloud system observed during TC4: Potential for enhancing nocturnal ice cloud retrievals, *Remote Sens.*, *4*, 3022–3054, doi:10.3390/rs4103022.
NASA (2015), CERES Terra & Aqua Edition 4a SSF cloud properties—Accuracy and validation, CERES Tech. Rep., 43 pp., Aug. 15. [Available online at http://www-pm.larc.nasa.gov/site/doc-library/260-ssf_cloud_prop_aqua_ed4.cal_val.pdf.]
Ou, S. C., K.-N. Liou, W. M. Gooch, and Y. Takano (1993), Remote sensing of cirrus cloud properties using advanced very-high resolution radiometer 3.7 and 10.9-μm channels, *Appl. Opt.*, *32*, 2171–2180.
Protat, A., J. Delanoë, E. J. O'Connor, and T. S. L'Ecuyer (2010), Evaluation of CloudSat and CALIPSO ice microphysical products using ground-based cloud radar and lidar observations, *J. Atmos. Oceanic Technol.*, *27*, 793–810.
Scarino, B. R., D. R. Doelling, P. Minnis, A. Gopalan, T. Chee, R. Bhatt, and C. Lukashin (2016), A web-based tool for calculating spectral band difference adjustment factors derived from SCIAMACHY hyperspectral data, *IEEE Trans. Geosci. Remote Sens.*, *54*, 2529–2542, doi:10.1109/TGRS.2015.2502904.

Smith, W. L., Jr. (2014), 4-D cloud properties from passive satellite data and applications to resolve the flight icing threat to aircraft, PhD dissertation, 165 pp., Univ. Wisconsin-Madison, Madison. [Available at http://www-pm.larc.nasa.gov/icing/pub/WLS-Dissertation.pdf.]

Stephens, G. L., et al. (2002), The CloudSat mission and A-Train, *Bull. Am. Meteorol. Soc.*, *83*, 1771–1790.

Stephens, G. L., et al. (2008), CloudSat mission: Performance and early science after the first year of operation, *J. Geophys. Res.*, *113*, D00A18, doi:10.1029/2008JD009982.

Szejwach, G. (1982), Determination of semi-transparent cirrus cloud temperature from infrared radiances: Application to Meteosat, *J. Appl. Meteorol.*, *21*, 384–393.

Tian, B., B. J. Soden, and X. Wu (2004), Diurnal cycle of convection, clouds, and water vapor in the tropical upper troposphere: Satellites versus a general circulation model, *J. Geophys. Res.*, *109*, D10101, doi:10.1029/2003JD004117.

Walther, A., A. K. Heidinger, and S. Miller (2013), The expected performance of cloud optical and microphysical properties derived from Suomi NPP VIIRS day/night band lunar reflectance, *J. Geophys. Res. Atmos.*, *118*, 13,230–13,240, doi:10.1002/2013JD020478.

Wielicki, B. A., et al. (1998), Clouds and the Earth's Radiant Energy System (CERES): Algorithm Overview, *IEEE Trans. Geosci. Rem. Sens.*, *36*, 1127–1141.

Winker, D. M., W. H. Hunt, and M. J. McGill (2007), Initial performance assessment of CALIOP, *Geophys. Res. Lett.*, *34*, L19803, doi:10.1029/2007GL030135.

Yang, P., G. W. Kattawar, G. Hong, P. Minnis, and Y. X. Hu (2008), Uncertainties associated with the surface texture of ice particles in satellite-based retrieval of cirrus clouds: Part II. Effect of particle surface roughness on retrieved cloud optical thickness and effective particle size, *IEEE Trans. Geosci. Remote Sens.*, *46*(7), 1948–1957, doi:10.1109/TGRS.2008.916472.

Yue, Q., and K.-N. Liou (2009), Cirrus cloud optical and microphysical properties determined from AIRS infrared spectra, *Geophys. Res. Lett.*, *36*, L05810, doi:10.1029/2008GL036502.